LBL-6264

OPTICAL QUADRUPOLE SUM-FREQUENCY GENERATION IN SODIUM VAPOR

Donald Stimson Bethune

Ph. D. thesis

May 1977

Prepared for the U. S. Energy Research and Development Administration under Contract W-7405-ENG-48

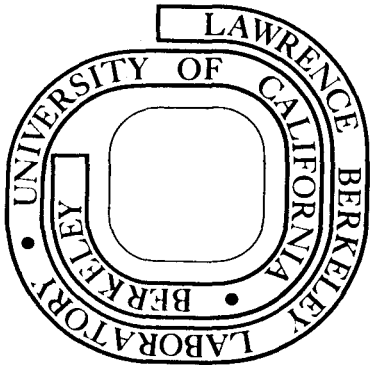

DISCLAIMER

LBL-6264

OPTICAL QUADRUPOLE SUM-FREQUENCY GENERATION IN SODIUM VAPOR

Donald Stimson Bethune

PhD Thesis

MAY 1977

Prepared for the U.S. Energy Research and
Development Administration under Contract W-7405-ENG-48

OPTICAL QUADRUPOLE SUM-FREQUENCY GENERATION IN SODIUM VAPOR

Donald Stimson Bethune

ABSTRACT

We show that second order nonlinear optical processes such as sum and difference generation can be observed in isotropic media, despite the fact that such processes are forbidden in the dipole approximation. A theoretical treatment of quadrupole sum and difference frequency generation is given, which includes the effects of spin-orbit splitting. The symmetry of the vapor is used to derive the form of the quadrupole susceptibility tensor, and the quadrupole moment tensor is then expressed as a scalar susceptibility multiplied by a tensor constructed directly from the input field polarization vectors. The expression shows that two non-collinear beams must be used. The effect of applying a magnetic field is derived. Expressions for phase matching and output power are found.

In sodium vapor we have observed quadrupole sum frequency generation (QSFG) of ultraviolet light. The output radiation showed very sharp resonant enhancement when $\omega_1 + \omega_2$ was tuned near the 3s → 4d quadrupole allowed transition of Na. The experimental results generally confirm the theoretical predictions. Deviations of the data from the simple theory can be satisfactorily accounted for by the effects of two photon saturation, induced index of refraction changes and single and multi-photon absorption.

We also show that by applying a D.C. electric field to the sodium vapor, interference effects between QSFG and D.C. induced, third-order sum-frequency generation may be observed, allowing an accurate determination of quadrupole matrix elements relative to dipole matrix elements of atoms.

We use this technique to measure the value of the 3s - 4d quadrupole transition moment of Na. Our result is $\langle 3s|zz/2|4d\rangle = (2.2 \pm 0.4)a_0^2$.

Finally, the generalization of the dipole forbidden susceptibilities to the case of quadrupole pumped processes is discussed, with difference frequency generation in Cs vapor considered as an example.

ACKNOWLEDGEMENTS

There are many people to whom I owe much for their friendship, support, and help during the course of this work.

I would especially like to thank

Professor Y. R. Shen for his guidance and help both during my research and in the preparation of this thesis;

Robert W. Smith, fellow student and co-worker throughout the experimental work, whose help was invaluable;

Dr. Eric Hanson, Dr. Bruce Patterson, Dr. Arnold Schmidt, and T. Ranganath, all of whom contributed their enthusiasm for life and science, and encouragement when I needed it;

My wife, Ann, for her patience and support, and for bringing Benjamin into the world and my life;

Rita Jones for being so cheerful and for typing the manuscript, and Gloria Pelatowski for preparing the figures.

I would also like to acknowledge the support of an NSF Graduate Fellowship during the first three years I was at Berkeley. This work was supported by the U.S. Energy Research and Development Administration.

OPTICAL QUADRUPOLE SUM-FREQUENCY GENERATION IN SODIUM VAPOR

TABLE OF CONTENTS

I. INTRODUCTION

The nonlinear optical properties of atomic vapors have received considerable attention in recent years. They have the potential to serve as sources of coherent radiation over a spectral range which extends from the extreme ultraviolet to the far-infrared.[1-5]

Their discrete spectra can be exploited to provide not only wide absorption-free regions but also strong resonance enhancement in their nonlinear susceptibilities. Thus, vacuum uv has been generated by third-harmonic generation,[1] and more recently, even fifth- and seventh-harmonic generation of 380 and 530 Å have been reported.[2] Tunable vacuum ultraviolet and infrared have also been produced by four wave mixing in metal vapors.[3] Other processes such as one-photon and two-photon stimulated electronic Raman scattering have been used for infrared generation.[4]

The common feature of all the processes mentioned above is their reliance on the odd-order dipole-allowed nonlinear susceptibilities. Even order susceptibilities are forbidden in the dipole approximation for centrosymmetric media. They are, however, nonvanishing if electric quadrupole and magnetic dipole matrix elements are taken into account in the susceptibilities. The subject has been described in numerous theoretical papers on second harmonic generation in centrosymmetric media.[6-12] Generally, one would expect that an n-th order forbidden process is not necessarily weaker than an (n + 1)th-order allowed process. Nevertheless, selection rules for the nth- and (n + 1)th-order processes may be different. For example, no bulk quadrupole second harmonic generation from a uniform centrosymmetric medium is possible. Experimental observations of surface second harmonic generation,[10,13-15] due to quadrupole and magne-

tic dipole effects show that it is quite weak. Hänsch and Toschek[16] have considered bulk sum- and difference-frequency generation due to second-order electric quadrupole or magnetic dipole nonlinear susceptibilities in a gaseous medium. With a collinear geometry they found that it is necessary to orient the atoms in order to have difference-frequency generation while sum-frequency generation is still forbidden for doubly resonant pumping. Pershan[6] has considered electric quadrupole and magnetic dipole contributions to the second-order nonlinear optical processes by using a phenomenological approach. He showed that isotropic materials with anomalous dispersion could be used to generate bulk second harmonic if two noncollinear pump beams were used. However, he concluded that this would be a very weak and possibly unobservable effect.

We have recently found that with the noncollinear beam geometry, a quadrupole-allowed second-order sum- or difference-frequency generation process in vapor can be as strong as a third-order wave-mixing process. In fact, both processes can be easily observed when the pump laser frequencies are tuned near single or/and double resonances of the atomic species. More recently, Flusberg et al.[17] have demonstrated that with an applied dc magnetic field, quadrupole sum-frequency generation and magnetic difference frequency generation in metal vapors can even be observed with a collinear beam geometry. In this paper, we give a more complete theory of quadrupole three-wave mixing in metal vapors. We also describe in detail our recent experiment of quadrupole sum-frequency generation (QSFG) in sodium vapor.

The body of the paper is divided into five sections. The first section of these gives a theoretical derivation of the second-order quadrupole susceptibility for one electron atoms, taking into account the spin-

orbit coupling and possible Zeeman coupling in the presence of a magnetic field. The effects of Doppler broadening and finite laser linewidth are discussed in a separate appendix. The phase matching condition for QSFG is then obtained and an expression for the total power output is derived. The second section describes the experimental arrangement and the observed experimental results on QSFG in sodium vapor. We compare these results with the theoretical predictions of the first section. The third section presents theory and experiment on saturation of two-photon absorption and self-defocusing of the pump beams as the limiting processes in QSFG. The effects of linear absorption due to both atoms and sodium dimers and multiphoton absorption are also discussed. The fourth section describes the use of interference between QSFG and dc electric-field-induced sum-frequency generation to determine experimentally the quadrupole transition matrix element relative to dipole matrix elements. The fifth section discusses other nonlinear processes depending on second-order quadrupole nonlinear susceptibilities. As an example, the susceptibility for quadrupole-allowed difference-frequency in Cesium vapor is calculated.

II. THEORY

A. Microscopic Expression of Second-Order Nonlinear Susceptibility

In the classical theory of radiation, the vector potential of the far field radiation generated by a current density distribution $\vec{j}(\vec{r}',\omega)e^{-i\omega t}$ with spatial Fourier components $\vec{j}(\vec{k}',\omega)$ is given by

$$\vec{A}(\vec{r},t) = (e^{i\vec{k}\cdot\vec{r}-i\omega t}/rc)\vec{j}(\vec{k},\omega), \quad k = n\omega/c. \tag{1}$$

For a collection of atoms or molecules with density N, $\vec{j}(\vec{k},\omega)$ can be expressed in terms of the Fourier component $\vec{J}(\vec{r}',\vec{k},\omega)$ of the current distribution of a single atom or molecule at $\vec{r}'$

$$\vec{j}(\vec{k},\omega) = \int e^{-i\vec{k}\cdot\vec{r}'} N \vec{J}(\vec{r}',\vec{k},\omega) d^3\vec{r}'. \tag{2}$$

Semiclassically, $\vec{J}(\vec{r}',\vec{k},\omega)$ is an expectation value obtained from

$$\vec{J}(\vec{r}',\vec{k},\omega) = \mathrm{Tr}[\rho(\vec{r}',\omega)\vec{j}_{op}(\vec{k},\omega)] \tag{3}$$

where $\rho(\vec{r}',\omega)$ is the density matrix operator with time dependence $e^{-i\omega t}$ of an atom or molecule at $\vec{r}'$, and $\vec{j}_{op}(\vec{k},\omega)$ is a current density operator. In a multipole expansion,[18,19] $\vec{j}_{op}(\vec{k},\omega)$ can be written as

$$\vec{j}_{op}(\vec{k},\omega) = -i\omega(\vec{p} - i\vec{k}\cdot\overleftrightarrow{q}) + ic\vec{k}\times\vec{m} + \ldots \tag{4}$$

where $\vec{p}$, $\overleftrightarrow{q}$ and $\vec{m}$ are the electric dipole, electric quadrupole, and magnetic dipole operators per atom. It is often convenient to define a general-

ized polarization vector as

$$\vec{P}(\vec{k},\omega) \equiv \frac{N\vec{J}(\vec{r}',\vec{k},\omega)}{-i\omega} . \tag{5}$$

Here, and from now on, the dependence of $\vec{P}(\vec{k},\omega)$ on $\vec{r}'$ is implicit. For sufficiently weak applied fields, $\vec{P}(\vec{k},\omega)$ can be expanded in a power series

$$\vec{P}(\vec{k},\omega) = \vec{P}^{(1)}(\vec{k},\omega) + \vec{P}^{(2)}(\vec{k},\omega) + \ldots \tag{6}$$

with

$$\begin{aligned} \vec{P}^{(1)}(\vec{k},\omega) &= \overleftrightarrow{\chi}^{(1)}(\vec{k},\omega,\vec{k}')\vec{E}(\vec{k}',\omega) \\ \vec{P}^{(2)}(\vec{k},\omega) &= \overleftrightarrow{\chi}^{(2)}(\vec{k},\omega = \omega_1 + \omega_2,\vec{k}_2,\omega_2,\vec{k}_1,\omega_1) : \vec{E}(\vec{k}_2,\omega_2)\vec{E}(\vec{k}_1,\omega_1) \end{aligned} \tag{7}$$

where $\overleftrightarrow{\chi}^{(1)}$ and $\overleftrightarrow{\chi}^{(2)}$ are the generalized first and second order susceptibility tensors. The microscopic expressions for $\overleftrightarrow{\chi}^{(1)}$ and $\overleftrightarrow{\chi}^{(2)}$ are obtained from perturbation calculation using the interaction Hamiltonian

$$\mathcal{H}_I = \sum_n - \vec{\pi}^{\dagger}(\vec{k}_n,\omega_n) \cdot \vec{E}(\vec{k}_n,\omega_n) \tag{8}$$

where

$$\vec{\pi}(\vec{k}_n,\omega_n) = \vec{\pi}^{\dagger}(-\vec{k}_n,-\omega_n) = \vec{p} - i\vec{k}_n \cdot \overleftrightarrow{q} - c\vec{k}_n \times \vec{m}/\omega_n + \ldots$$

for a set of monochromatic fields with frequencies ω_n.

The second-order susceptibility may be expressed[19,20]

$$\chi^{(2)}_{hij}(\vec{k},\omega = \omega_1 + \omega_2,\vec{k}_2,\omega_2,\vec{k}_1,\omega_1) = \frac{N}{2\hbar^2} P \sum_{rst} \frac{\langle r|\pi_h(\vec{k},\omega)|t\rangle\langle t|\pi_i(-\vec{k}_2,-\omega_2)|s\rangle\langle s|\pi_j(-\vec{k}_1,-\omega_1)|r\rangle\rho^0_{rr}}{(\omega_{tr} - \omega_1 - \omega_2)(\omega_{sr} - \omega_1)} \tag{9}$$

where ρ^0_{rr} is the equilibrium population of the state $|r\rangle$, and P indicates a sum of six terms obtained from permuting the three sets of quantities $[(h,-\vec{k},-\omega),\ (i,\vec{k}_2,\omega_2),\ (j,\vec{k}_1,\omega_1)]$.

Here, for quadrupole second-order sum -frequency generation, we are particularly interested in the susceptibility

$$\overleftrightarrow{\chi}^{(2)} = \frac{NP}{2\hbar^2} \sum_{r,s,t} \frac{\langle r|-i\vec{k}\cdot\overleftrightarrow{q}|t\rangle\langle t|\vec{p}|s\rangle\langle s|\vec{p}|r\rangle\rho^0_{rr}}{(\omega_{tr} - \omega_1 - \omega_2)(\omega_{sr} - \omega_1)} \equiv -i\vec{k}\cdot\overleftrightarrow{\chi}^{(Q)}. \tag{10}$$

Physically, $\overleftrightarrow{Q}(\omega) = \overleftrightarrow{\chi}^{(Q)} : \vec{E}(\omega_2)\vec{E}(\omega_1)$ is a sum-frequency quadrupole polarization induced by the nonlinear mixing of $\vec{E}(\omega_1)$ and $\vec{E}(\omega_2)$. The radiation pattern of a quadrupole $\overleftrightarrow{Q}\, d^3x$ with only $Q_{yz} = Q_{zy} \neq 0$ is shown in Fig. 1 as an example. To include damping in Eqs. (9) and (10) we need to insert a damping factor $\pm i\gamma_{mn}$ into each denominator with the resonant frequency ω_{mn}, with the signs chosen such that the denominators vanish only when ω_1 or ω_2 is in the lower half of the complex ω plane.[20]

From symmetry considerations, the nonvanishing elements of $\overleftrightarrow{\chi}^{(Q)}$ are $\chi^{(Q)}_{1111}$, $\chi^{(Q)}_{1122}$, $\chi^{(Q)}_{1212} = \chi^{(Q)}_{2112}$, with $\chi^{(Q)}_{1111} = \chi^{(Q)}_{1122} + \chi^{(Q)}_{1212} + \chi^{(Q)}_{2112}$. In addition, a sum of equal diagonal elements of $\overleftrightarrow{Q}$ cannot radiate because its effective polarization $(-i\vec{k}\cdot\overleftrightarrow{Q})$ is parallel to $\vec{k}$. Therefore, we can

define $\overleftrightarrow{Q}$ as a traceless tensor by using $q_{ij} = \frac{1}{2} e(r_i r_j - r^2 \delta_{ij}/3)$. We then have $\chi^{(Q)}_{1111} + \chi^{(Q)}_{2211} + \chi^{(Q)}_{3311} = 0$, and hence, $\chi^{(Q)}_{1122} = -\frac{1}{2}\chi^{(Q)}_{1111}$ and $\chi^{(Q)}_{1212} = \frac{3}{4}\chi^{(Q)}_{1111}$. It is now easy to show that

$$\vec{P}(\vec{k},\omega) = -i2\chi^{(Q)}_{1212}\{(\vec{k}\cdot\vec{E}(\omega_1))\vec{E}(\omega_2) + (\vec{k}\cdot\vec{E}(\omega_2))\vec{E}(\omega_1) - \frac{2}{3}\vec{k}(\vec{E}(\omega_1)\cdot\vec{E}(\omega_2))\}. \tag{11}$$

The dot products show that collinear QSFG is not possible since we must have both $\vec{E}(\omega_i) \perp \vec{k}$ and $\vec{P}(\vec{k},\omega) \perp \vec{k}$.

B. Evaluation of Quadrupole Nonlinear Susceptibility $\overleftrightarrow{\chi}^{(Q)}(\omega = \omega_1 + \omega_2)$

We now want to calculate the value of the quadrupole nonlinear susceptibility $\overleftrightarrow{\chi}^{(Q)}$ for one-electron atoms, including the effect of spin-orbit coupling. We shall also consider the effect of an applied magnetic field. Such a field destroys the isotropic symmetry so that Eq. (11) no longer holds.

The evaluation of $\overleftrightarrow{\chi}^{(Q)}$ in Eq. (10) for one-electron atoms is most easily done in spherical coordinates[21] ($\hat{u}_{\pm1} = \mp(\hat{e}_x \pm i\hat{e}_y)/\sqrt{2}$ and $\hat{u}_0 = \hat{e}_z$). Using the Greek indices to indicate the spherical coordinates, the spherical tensor components $\chi^{(Q)}_{\gamma\delta\alpha\beta}$ are related to the Cartesian tensor components $\chi^{(Q)}_{\ell mjk}$ by the relation

$$\chi^{(Q)}_{\gamma\delta\alpha\beta} = (\hat{u}_\gamma\cdot\hat{e}_\ell)(\hat{u}_\delta\cdot\hat{e}_m)(\hat{u}_\alpha\cdot\hat{e}_j)(\hat{u}_\beta\cdot\hat{e}_k)\chi^{(Q)}_{\ell mjk}, \tag{12}$$

where we use the summation convention. We can further simplify the calculation by using the standard quadrupole components[21] q_M with M = 2,1, 0,-1,-2 instead of $q_{\gamma\delta}$.

$$\begin{pmatrix} q_2 \\ q_1 \\ q_0 \\ q_{-1} \\ q_{-2} \end{pmatrix} = \frac{e}{2} \begin{pmatrix} r_{+1}r_{+1} \\ (r_{+1}r_0 + r_0r_{+1})/\sqrt{2} \\ (r_{+1}r_{-1} + r_0r_0 + r_{-1}r_{+1})/\sqrt{6} \\ (r_0r_{-1} + r_{-1}r_0)/\sqrt{2} \\ r_{-1}r_{-1} \end{pmatrix} \tag{13}$$

where, for example, $r_{+1} = \hat{u}_1 \cdot \vec{r} = -(x + iy)/\sqrt{2}$. We have from Eq. (10)

$$\chi^{(Q)}_{M\alpha\beta} = \frac{N}{2\hbar^2} P \sum_{a,b,c} \rho^0_{aa} \frac{\langle a|q_M|c\rangle\langle c|p_\alpha|b\rangle\langle b|p_\beta|a\rangle}{D_{ca}(\omega_1 + \omega_2)D_{ba}(\omega_1)} \tag{14}$$

which is connected to $\chi^{(Q)}_{\gamma\delta\alpha\beta}$ by the relations

$$\begin{aligned} \chi^{(Q)}_{M\alpha\beta} &= \sum_{\gamma,\delta} \langle 1,1\gamma\delta|2M\rangle \chi^{(Q)}_{\gamma\delta\alpha\beta} \\ \chi^{(Q)}_{\gamma\delta\alpha\beta} &= \langle 1,1\gamma\delta|2M\rangle \chi^{(Q)}_{M\alpha\beta} \qquad (M = \gamma + \delta) \end{aligned} \tag{15}$$

and where $D_{ab}(\omega) \equiv \omega_{ab} - \omega$ and $\langle 1,1\gamma\delta|2M\rangle$ is a Clebsch-Gordan coefficient. It can be shown that for the spherically symmetric case

$$\chi^{(Q)}_{M\alpha\beta} = (-1)^M \langle 1,1\alpha\beta|2-M\rangle \chi^{(Q)}_{2,-1,-1}. \tag{16}$$

Thus, from Eqs. (12), (15), and (16), we can express $\chi^{(Q)}_{\ell mjk}$ in terms of $\chi^{(Q)}_{2,-1,-1}$. In our case, we have only one independent element of $\chi^{(Q)}_{\ell mjk}$. We find

$$\chi^{(Q)}_{1212} = \chi^{(Q)}_{1221} = -\frac{3}{2}\chi^{(Q)}_{1122} = \frac{3}{4}\chi^{(Q)}_{1111} = \frac{1}{2}\chi^{(Q)}_{2,-1,-1}. \tag{17}$$

We are now left with the evaluation of $\chi^{(Q)}_{2,-1,-1}$, and in particular the matrix elements in $\chi^{(Q)}_{2,-1,-1}$. Following the notation of Shore and Menzel[22] we can write $\vec{p}$ and $\overleftrightarrow{q}$ in terms of the Racah tensors $C^{(K)}$.

$$p_\alpha = erC^{(1)}_\alpha$$

$$q_M = (er^2/\sqrt{6})C^{(2)}_M \tag{18}$$

$$C^{(K)}_M = [4\pi/(2K+1)]^{\frac{1}{2}} Y_{KM}$$

where Y_{KM} are the spherical harmonics. Then, the matrix elements of p_α and q_M between states specified by the quantum numbers n, ℓ, s, j, and m_j can be reduced using the Wigner-Eckart theorem, which allows us to write

$$\langle n'\ell'j'm_j'|f(r)C^{(K)}_M|n\ell jm_j\rangle = [\langle jKm_jM|j'm_j'\rangle/(2j'+1)^{\frac{1}{2}}]\langle n'\ell'j'\|f(r)C^{(K)}\|n\ell j\rangle. \tag{19}$$

Here, since the spin quantum numbers are always ½, we have suppressed them. The double bar matrix element can be further reduced in terms of the Racah coefficients $W(\frac{1}{2}j'\ell K;\ell'j)$ and the Clebsch-Gordan coefficients[22]:

$$\langle n'\ell'j'\|f(r)C^{(K)}\|n\ell j\rangle = [(2j'+1)(2j+1)]^{\frac{1}{2}}W(\tfrac{1}{2}j'\ell K;\ell'j)\langle n'\ell'\|f(r)C^{(K)}\|n\ell\rangle$$

$$\langle n'\ell'\|f(r)C^{(K)}\|n\ell\rangle = (2\ell'+1)^{\frac{1}{2}}\langle \ell K00|\ell'0\rangle\langle n'\ell'\|f(r)\|n\ell\rangle \tag{20}$$

$$\langle n'\ell'\|f(r)\|n\ell\rangle \equiv \int_0^\infty P_{n'\ell'}(r)f(r)P_{n\ell}(r)dr$$

where $P_{n\ell}(r)/r$ is the radial wave function of the state $|n\ell\rangle$.

Assuming unoriented atoms initially in the ground state $|n''s\tfrac{1}{2}m''>$ and using the tabulated Clebsch-Gordan and Racah coefficients,[23] we obtain

$$\chi^{(Q)}_{2,-1,-1} = \frac{Ne^3}{2\hbar^2} P' \sum_{n,n'} \left\{ \frac{I^{nn'n''}_{sdps}}{15} \left[\frac{9}{15} A^{nn'}_{\frac{5}{2},\frac{3}{2}} + \frac{1}{15} A^{nn'}_{\frac{3}{2},\frac{3}{2}} + \frac{5}{15} A^{nn'}_{\frac{3}{2},\frac{1}{2}} \right] + \frac{I^{nn'n''}_{spps}}{15} \left[\frac{1}{3} B^{nn'}_{\frac{3}{2},\frac{3}{2}} + \frac{1}{3} B^{nn'}_{\frac{3}{2},\frac{1}{2}} + \frac{1}{3} B^{nn'}_{\frac{1}{2},\frac{3}{2}} \right] \right\} \tag{21}$$

where

$$I^{nn'n''}_{sdps} = <n''s\|r^2\|nd><nd\|r\|n'p><n'p\|r\|n''s>$$

$$I^{nn'n''}_{spps} = <n''s\|r\|np><np\|r^2\|n'p><n'p\|r\|n''s>$$

$$A^{nn'}_{jj'} = \left[D_{nd_j}(\omega) \cdot D_{n'p_{j'}}(\omega_1) \right]^{-1} + \left[D_{nd_j}(-\omega) \cdot D_{n'p_{j'}}(-\omega_1) \right]^{-1}$$

$$B^{nn'}_{jj'} = \left[D_{np_j}(-\omega_2) \cdot D_{n'p_{j'}}(\omega_1) \right]^{-1}$$

and P' indicates the sum of two terms obtained from permutation of ω_1 and ω_2. The resonant frequency in the denominator $D_{n\ell_j}$ is $\omega_{n\ell_j,n''s_{\frac{1}{2}}}$. Knowing the values of the radial integrals in $I^{nn'n''}_{sdps}$ and $I^{nn'n''}_{spps}$, we can then evaluate $\overleftrightarrow{\chi}^{(Q)}$ numerically. As an example we consider the case of sodium vapor with $N = 10^{16}/cm^3$, $\omega_{3p_{\frac{1}{2}}} - \omega_1 = 10\ cm^{-1}$, and $\omega_{4d} - \omega_1 - \omega_2 = 0.25\ cm^{-1}$. Using the radial integrals $<n'\ell'\|r\|n\ell>$ obtained from Ref. 24 and the calculated values of $<n'\ell'\|r^2\|n\ell>$ from Ref. 25, we find the susceptibility for QSFG is $\chi^{(Q)}_{2,-1,-1} = 1.2 \times 10^{-14}$ esu. The terms involving $B^{nn'}_{jj'}$ in Eq. (21) can give resonant p → p quadrupole difference frequency generation (QDFG) when ω_2 is replaced by $-\omega_2$ and $\vec{E}(\omega_2)$ by $\vec{E}^*(\omega_2)$. As an ex-

ample, with $N = 10^{16}/cm^3$, $\omega_{3p_{\frac{1}{2}}} - \omega_1 = 10\ cm^{-1}$ and $\omega_{4p_{3/2}} - \omega_2 = -2\ cm^{-1}$, the susceptibility for p → p QDFG will be $\chi^{(Q)} = 7.55 \times 10^{-16}$ esu.

It is quite simple to extend the calculation to include the effect of an applied D.C. magnetic field $\vec{B}$. Taking $\vec{B}$ along $\hat{z}$, the transition frequency between $|n\ell jm_j>$ and $|n'\ell'j'm_{j'}>$ now becomes

$$\omega^{(m_j,m_{j'})}_{n\ell_j,n'\ell'_{j'}} = \omega^{0}_{n\ell_j,n'\ell'_{j'}} + \frac{\mu_B B}{\hbar}(g_j m_j - g_{j'} m_{j'}) \qquad (22)$$

where μ_B is the Bohr magneton and g_j is the Landé g factor. Since Zeeman splittings are usually small, the slight changes in the denominators in Eq. (14) will affect the value of $\overleftrightarrow{\chi}^{(Q)}$ only near resonance.

For illustration, suppose that $\omega_1 + \omega_2 \approx \omega_{4d}$ in QSFG, but that ω_1 is sufficiently far from resonance that the change in the 3s → 3p denominator can be neglected. In the limit of weak magnetic fields, we consider only the linear effect of the Zeeman splitting of $\omega_{4d,3s}$ on $\overleftrightarrow{\chi}^{(Q)}$. We find

$$\overleftrightarrow{\chi}^{(Q)} = \overleftrightarrow{\chi}^{(Q)}(0) + \overleftrightarrow{\Delta\chi}^{(Q)}(B) \qquad (23)$$

where $\overleftrightarrow{\Delta\chi}^{(Q)}(B)$ is linear in B, and is given by

$$\Delta\chi^{(Q)}_{M\alpha\beta}(B) = (-1)^M \frac{M}{2} <1,1\alpha\beta|2\text{-}M>\Delta\chi^{(Q)}_{2,-1,-1}(B) \qquad (24)$$

with

$$\Delta\chi^{(Q)}_{2,-1,-1}(B) \cong \frac{Ne^3}{2\hbar^2} \frac{I^{4,3,3}_{sdps}}{15} \left(\frac{\mu_B B}{\hbar}\right) \times$$

$$p' \left[\frac{96}{75} \frac{A^{4,3}_{\frac{5}{2},\frac{3}{2}}}{D_{4d_{\frac{5}{2}}}(\omega)} + \frac{11}{75} \frac{A^{4,3}_{\frac{3}{2},\frac{3}{2}}}{D_{4d_{\frac{3}{2}}}(\omega)} + \frac{55}{75} \frac{A^{4,3}_{\frac{3}{2},\frac{1}{2}}}{D_{4d_{\frac{3}{2}}}(\omega)} \right] . \tag{25}$$

As an example consider the case where $\vec{E}_1 \| \vec{B} \| \hat{x}$ and $\vec{E}_2 \| \hat{y}$. Eqs. (23) and (24) lead to

$$P_y = -\, i(\vec{k} \cdot \hat{x}) \chi^{(Q)}_{2,-1,-1}(0) E_1 E_2$$

$$P_x = -\, (\hat{k} \cdot \hat{z})(\tfrac{1}{2}) \Delta\chi^{(Q)}_{2,-1,-1}(B) E_1 E_2 . \tag{26}$$

For collinear QSFG along $\hat{z}$, the above equations show that both P_x and P_y vanish at B = 0 but $P_x \neq 0$ when $B \neq 0$, confirming that only magnetic-field-induced QSFG is possible.[17]

The magnitudes of $\chi^{(Q)}_{2,-1,-1}$ and $\chi^{(Q)}_{2,-1,-1}(B)$ at $\omega_1 + \omega_2 = \omega_{4d}$ with Doppler broadening are approximately in the ratio

$$|\chi^{(Q)}_{2,-1,-1}(B)| / |\chi^{(Q)}_{2,-1,-1}| \approx \frac{\mu_B B}{\hbar \Omega_{ds}} . \tag{27}$$

At one torr, the Doppler width of the 4d - 3s transition $\Omega_{ds} \simeq .085\ cm^{-1}$ and this ratio is less than one until B ~ 2 kilogauss. Comparable QSFG may be obtained with B ~ 10 Gauss however (see Appendix A).

In a similar way a magnetically induced $\Delta\chi^{(Q)}(B)$ for the $p \rightarrow p$ term

of the susceptibility can be calculated. In their magnetically induced DFG experiment, Flusberg, et al.[17] tuned two collinear lasers near the $6^2P_{1/2} - 7^2S_{1/2}$ and $6^2P_{3/2} - 7^2S_{1/2}$ transitions of thallium vapor in a transverse magnetic field, and observed a collinear difference frequency beam near $\omega_{6^2P_{1/2}-6^2P_{3/2}} = 7793\ \text{cm}^{-1}$, due mostly to magnetic dipole radiation.

C. Phase Matching and Output Power of Quadrupole Sum-Frequency Generation

We assume two single mode pump beams with Gaussian profiles, $\vec{k}_1 \times \vec{k}_2 \| \hat{y}$ and $\vec{k}_1 + \vec{k}_2 \| \hat{z}$. If diffraction can be neglected in the interaction region, we can write the two pump fields as

$$\vec{E}(\omega_{1,2}) = \vec{\mathcal{E}}_{1,2} \exp(i\vec{k}_{1,2} \cdot \vec{r} - \rho^2_{1,2}/2\sigma^2_{1,2}) \tag{28}$$

where

$$\rho_1^2 = y^2 + (x \cos\theta_1 - z \sin\theta_1)^2$$

$$\rho_2^2 = y^2 + (x \cos\theta_2 + z \sin\theta_2)^2 .$$

θ_i is the angle between $\vec{k}_i$ and $\hat{z}$, and both angles are defined to be positive. Then, from Eq. (11), we have

$$\vec{P}(\vec{k},\omega) = -i\chi^{(Q)}_{2,-1,-1}[\vec{\mathcal{E}}_1(\vec{k}\cdot\vec{\mathcal{E}}_2) + \vec{\mathcal{E}}_2(\vec{k}\cdot\vec{\mathcal{E}}_1)] \times \exp\left[i(\vec{k}_1+\vec{k}_2)\cdot\vec{r} - \frac{\rho_1^2}{2\sigma_1^2} - \frac{\rho_2^2}{2\sigma_2^2}\right] \tag{29}$$

where we discard the term in Eq. (11) $\propto \vec{k}$ since it cannot radiate along $\vec{k}$. Using this expression for $\vec{P}(\vec{k},\omega)$ with Eqs. (5), (2), and (1) yields a vector potential

$$\vec{A}(\vec{r},t) = \frac{e^{ikr-i\omega t}}{rc}\left(-\omega\chi^{(Q)}_{2,-1,-1}[\vec{\mathcal{E}}_1(\vec{k}\cdot\vec{\mathcal{E}}_2) + \vec{\mathcal{E}}_2(\vec{k}\cdot\vec{\mathcal{E}}_1)]\right)\times \tag{30}$$

$$\left(\frac{\pi^3}{(\alpha_1+\alpha_2)\alpha_1\alpha_2\sin^2(\theta_1+\theta_2)}\right)^{\frac{1}{2}} \exp\left[-\frac{\Delta k_y^2}{4a} - \frac{d\Delta k_x^2 + b\Delta k_z^2 + g\Delta k_x\Delta k_z}{4\alpha_1\alpha_2\sin^2(\theta_1+\theta_2)}\right]$$

where we have defined

$$\alpha_1 = 1/2\sigma_1^2 \qquad \alpha_2 = 1/2\sigma_2^2$$

$$a = \alpha_1 + \alpha_2 \qquad b = \alpha_1\cos^2\theta_1 + \alpha_2\cos^2\theta_2$$

$$d = \alpha_1\sin^2\theta_1 + \alpha_2\sin^2\theta_2 \qquad g = \alpha_1\cos\theta_1\sin\theta_1 - \alpha_2\cos\theta_2\sin\theta_1$$

and $\Delta\vec{k} = \vec{k} - (\vec{k}_1 + \vec{k}_2)$.

For arbitrary linear polarizations with ϕ_1 and ϕ_2 the angles between $\vec{\mathcal{E}}_1$ and $\hat{y}$ and $\vec{\mathcal{E}}_2$ and $\hat{y}$ respectively, the polarization in Eq. (29) has x and y components

$$P_x = -i\chi^{(Q)}_{2,-1,-1}kE(\omega_1)E(\omega_2)[\sin\phi_1\sin\phi_2\sin(\theta_2-\theta_1)]$$

$$P_y = -i\chi^{(Q)}_{2,-1,-1}kE(\omega_1)E(\omega_2)[\sin\phi_1\cos\phi_2\sin\theta_1 - \sin\phi_2\cos\phi_1\sin\theta_2]. \tag{31}$$

Since $k_1\sin\theta_1 = k_2\sin\theta_2$, if $k_1 \simeq k_2$ then $\theta_1 \simeq \theta_2$. Consequently $P_x \propto (\theta_2 - \theta_1)$ becomes very small, while $P_y \propto \sin\theta_1\sin(\phi_1 - \phi_2)$ and is a maximum if $(\phi_1 - \phi_2) = \pm 90°$. Assuming $k_2 > k_1$, the case with $\vec{\mathcal{E}}_1 \perp (\vec{k}_1 \times \vec{k}_2)$ and $\vec{\mathcal{E}}_2 \parallel \vec{k}_1 \times \vec{k}_2$ gives the optimum output power, and output polarization parallel to $\vec{k}_1 \times \vec{k}_2 \parallel \hat{y}$. The sum frequency output power is given by

$$\mathcal{P}(\omega) = \int \frac{\omega^2}{2\pi c} |\vec{A}|^2 \, r^2 \, d\Omega \tag{32}$$

which can be readily integrated to give for the optimum case

$$\mathcal{P}(\omega) = \frac{4\pi^3\omega^4}{c^5} |\chi^{(Q)}_{2,-1,-1}|^2 \mathcal{S}(\omega_1)\mathcal{S}(\omega_2) e^{-\Delta k_z^2/2d} \cdot F \tag{33}$$

where the geometric overlap factor F is defined

$$F = \frac{4\sin^2\theta_1}{\sin(\theta_1 + \theta_2)} \left[\frac{\alpha_1\alpha_2}{(\alpha_1 + \alpha_2)(\alpha_1\sin^2\theta_1 + \alpha_2\sin^2\theta_2)} \right]^{1/2}$$

$$\simeq \sqrt{1 - \left(\frac{\alpha_1 - \alpha_2}{\alpha_1 + \alpha_2}\right)^2} \quad \text{if } \theta_1 \simeq \theta_2 \tag{34}$$

$$\simeq 1 \quad \text{if } \theta_1 \simeq \theta_2 \text{ and } \alpha_1 \simeq \alpha_2.$$

We can find the phase-matching angle $\theta_p = \theta_{1p} + \theta_{2p}$ from the phase-matching condition $\Delta k_z = 0$. We obtain, using $\omega_3 = \omega_1 + \omega_2$,

$$(1 - \cos\theta_p) \approx \theta_p^2/2 = (\Delta n_1 - \Delta n_3)\left(1 + \frac{\omega_1}{\omega_2}\right) + (\Delta n_2 - \Delta n_3)\left(1 + \frac{\omega_2}{\omega_1}\right) \tag{35}$$

where $\Delta n_i \equiv n(\omega_i) - 1$, and higher order terms in the Δn_i have been neglected. Since $\vec{k} \parallel \hat{z}$ we also have $(\theta_{1p} - \theta_{2p})/\theta_p \cong (k_2 - k_1)/(k_2 + k_1)$. The refractive indices can be computed from a standard Sellmeier formula. From Eq. (35), it is clear we must utilize anomalous dispersion to achieve phase matching, as was noticed by Pershan[6] for the second harmonic case. If we let $\theta = \theta_1 + \theta_2$, we can also write the phase matching factor in terms of the phase-mismatch angle $\Delta\theta = (\theta - \theta_p)$:

$$\exp(-\Delta k_z^2/2d) = \exp(-\Delta\theta^2/2\sigma_\theta^2) \tag{36}$$

where

$$\sigma_\theta^2 = (1/2\sigma_1^2 k_1^2 + 1/2\sigma_2^2 k_2^2). \tag{37}$$

Although the theory given in this section neglects Doppler broadening and finite laser linewidth, these effects can be included in a fairly straight-forward way. This is done in an Appendix. It is shown there that for the case where $\gamma_{ds} << \Omega_{ds} << \gamma_L$, when $|\chi^{(Q)}|^2$ is evaluated to find the output power, we should use an effective susceptibility near resonance $|\chi_{eff}^{(Q)}|^2$, which has frequency dependence $\dfrac{\sqrt{2\pi}\ \gamma_L/\Omega_{ds}}{(\omega_{4d} - \omega_1 - \omega_2)^2 + \gamma_L^2}$ (where γ_L is the sum of the laser linewidths and $\Omega_{ds} \simeq .085\ cm^{-1}$ is the 4d → 3s Doppler width), instead of the dependence $|1/(\omega_{4d} - \omega_1 - \omega_2 - i\gamma)|^2$ (where γ is the natural linewidth) obtained from the theory given above.

III. EXPERIMENT

A. Choice of Atomic Vapor

To observe QSFG most easily, we should take advantage of the resonant enhancement of $\overleftrightarrow{\chi}^{(Q)}$. We selected atomic sodium vapor as our medium because it has levels well matched to our flash-pumped tunable dye lasers. In addition, the quadrupole susceptibility can be calculated theoretically, since the necessary atomic parameters are well known. A partial level diagram for sodium is shown in Fig. 2 with the sum frequency process we have investigated indicated schematically. For $N = 10^{16}/cm^3$, $\gamma_L = .25\ cm^{-1}$, $\omega_{4d} - \omega_1 - \omega_2 = 0$ and $\Delta\omega_1 \equiv \omega_{3p_{\frac{1}{2}}} - \omega_1 = 10\ cm^{-1}$, the effective nonlinear susceptibility $\chi^{(Q)}_{2,-1,-1}$ defined at the end of Section II is 3.05×10^{-14} esu. Using Eq. (33), we estimate an output power $P(\omega_1 + \omega_2) = [P(\omega_1)P(\omega_2)/(11.7 \times 10^6)]$ watts at exact phase matching, or about 1W for two 4 KW input beams.

B. Experimental Arrangement

The experimental arrangement is shown in Fig. 3. Two flash-pumped dye lasers provided ~ 600 nsec, linearly polarized pulses of light, with peak powers of about 1 - 5 KW. One laser used with Rhodamine 6G in ethanol was tunable between 5700 Å and 6300 Å, while the other with Rhodamine 6G in a water-hexafluoroisopropanol (2:1) solution was tunable between 5600 Å and 6100 Å. Both lasers were tuned with interference filter-etalon assemblies and had linewidths of ≃ 4 Ghz. A motor rotated the etalon to allow continuous tuning. The two lasers were fired synchronously. The relative jitter in the overlapping of the two pulses was about 100 nsec. The pulse shapes and temporal overlap of the pulses were monitored with a photodiode (PD 3) and an oscilloscope. Two long focal-length lenses

(f_1 = 40 cm, f_2 = 50 cm) focused the beams to a common 0.25 mm spot at the center of a heat pipe oven.[26] The angle of intersection could be finely adjusted by giving beam 1 a parallel displacement before focusing. With careful adjustment of the position of the lens L1, the actual point of intersection remained fixed.

The heat pipe oven was constructed from type 347 stainless steel tubing 20.3 cm long, 3.18 cm in diameter, and was flattened somewhat to a cross section of 1.9 cm × 4.5 cm. The actual sodium vapor zone was about 10 cm long and was fixed by water-cooled Aℓ flanges clamped to the heat pipe. The wick was made of several layers of 100 mesh type 304 stainless steel cloth. A glass input window and a fused silica output window were used on the heat pipe. The pressure was set by the He buffer gas, and was stabilized against outgassing by pumping continuously with a liquid-nitrogen-cooled zeolite pump, which could not pump He. The heat pipe was operated between 0.1 and 30 torr. At the higher pressures, molecular absorption due to sodium dimers became significiant and made the vapor appear very dark and violet in color.

The output radiation was filtered against fluorescence and scattered pump radiation by using a Corning 7-54 filter and a Jarrel-Ash ¼ m monochrometer with 500 μ slits, and was detected by a UV-sensitive photomultiplier. The output current from the photomultiplier was fed directly into a gated electrometer[27] which integrated the current with a time constant of about 5 sec. The output signal was then displayed on a chart recorder. Additional photodetectors (PD1 and PD2) and gated electrometers were used simultaneously to measure the average laser powers.

C. Results

In our experiments, we could vary the laser frequencies, the laser powers, the laser polarizations, the beam intersection angle θ, and the sodium vapor pressure (or density N).

When $\omega_1 + \omega_2$ was tuned near ω_{4d} (34548.8 cm^{-1}), and θ was set near the phase matching angle θ_p for $N \sim 10^{16}$ cm^{-3}, a strong ultraviolet beam at $\omega = \omega_1 + \omega_2$ was detected. Its linewidth was found to be spectrometer limited ($\Delta\lambda < 3$ Å). The output beam was highly directional and had a divergence angle less than 10 mrad. In contrast, the strong ultraviolet fluorescence from 5p → 3s and 4p → 3s transitions (λ = 2853 Å and 3304 Å respectively) appeared in all directions and was drastically reduced when a small aperture was inserted in front of the photodetector.

The polarization characteristics of the output were also measured. With $\vec{E}(\omega_1) \parallel \vec{k}_1 \times \vec{k}_2$ and $\vec{E}(\omega_2) \perp \vec{k}_1 \times \vec{k}_2$ the output was strong and polarized along $\vec{k}_1 \times \vec{k}_2$, as predicted by Eq. (11). When $\vec{E}_1 \parallel \vec{E}_2$, the signal was weaker by several orders, again in agreement with the prediction of Eq. (31). Errors in setting the polarizers and analyzers were probably responsible for the residual signal.

The resonance behavior of QSFG was investigated by keeping ω_1 fixed and θ adjusted to the phase matching value θ_p, and then scanning ω_2 over a narrow range with $\omega_1 + \omega_2 \simeq \omega_{4d}$. Phase matching should remain unchanged for the small tuning of ω_2. The sharp resonance observed when $\omega_1 + \omega_2$ goes through ω_{4d} is shown in Fig. 4. This curve was taken at low input powers ($\mathcal{P}(\omega_1) \cong 2W$ and $\mathcal{P}(\omega_2) \cong 25W$) and had a width of .25 cm^{-1}, which was dominated by our laser linewidths. The Doppler width for the resonance is narrower ($\sim .086$ cm^{-1}). This resonant enhancement was most important for strong sum-frequency output. At resonance, we could easily detect the output even if ω_1 was detuned from $\omega_{3p_{1/2}}$ by ~ 100 cm^{-1} or more,

but away from resonance, the output signal quickly disappeared.

To study phase matching of QSFG, the beam intersection angle θ was scanned continuously while other parameters were fixed. A typical phase matching curve is shown in Fig. 5, together with the corresponding theoretical curve obtained from Eqs. (36) and (33) with σ_θ = .92 mrad. This value of σ_θ is in reasonable agreement with the value 1.1 mrad calculated from Eq. (37) using the measured values of the beam waists. The peak of the experimental curve appears at an angle θ_p within 1.2 mrad of the value predicted from Eq. (35) using the measured Na vapor pressure to calculate $\Delta n_{1,2}$ from the Sellmeier formula. To check Eq. (35) in more detail, a set of measurements of θ_p was made for various densities and detunings $\Delta\omega_1$. The results are shown in Fig. 6, in comparison to the curves of θ_p vs N and $\Delta\omega_1$ calculated from Eq. (35). No adjustable parameters were used in the calculation. The agreement between theory and experiment is within 4 mrad in all cases.

In Fig. 7, we show the results of a measurement of sum-frequency output $\mathcal{P}(\omega_3)$ as a function of the input laser powers at phase matching. As expected, $\mathcal{P}(\omega_3) \propto \mathcal{P}(\omega_2)$ for fixed $\mathcal{P}(\omega_1)$ throughout the measured range. For sufficiently low $\mathcal{P}(\omega_1)$, $\mathcal{P}(\omega_3)$ is also proportional to $\mathcal{P}(\omega_1)$. However, at higher $\mathcal{P}(\omega_1)$, $\mathcal{P}(\omega_3)$ reaches a maximum and then begins to fall again as $\mathcal{P}(\omega_1)$ is further increased. This was due to resonant saturation, self-defocusing, and induced phase-mismatch. We shall discuss these effects in more detail in the next section.

Since the susceptibility $\chi^{(Q)}$ is proportional to the atomic density N, we expect $\mathcal{P}(\omega_3)$ at phase matching should increase as N^2. Measurements of $\mathcal{P}(\omega_3)$ vs N for two values of $\Delta\omega_1$ are shown in Fig. 8. Over a limited range, the expected N^2 dependence holds. The larger output for the case

of smaller $\Delta\omega_1$ demonstrates qualitatively the additional resonant enhancement due to $\Delta\omega_1$ in $\chi^{(Q)}$. The sharp decreases of the output observed at higher densities are due to atomic absorption, which will be discussed in the next section.

Thus, the predictions of Eq. (33) for sum-frequency generation are generally confirmed by our experimental results. Besides the two deviations from the elementary theory noted above, several additional complications were observed. As $\Delta\omega_1$ detuning was decreased, or N increased, the ω_1 beam traversing the cell was strongly defocused. This defocusing was accompanied by a substantial increase in the width of the phase matching curve and a decrease in the output power. Also, as the product, $I(\omega_1)I(\omega_2)$ became large, a significant broadening of the resonance curve $\mathcal{P}(\omega_3)$ vs ω_2 was observed, again accompanied by a reduction in $\mathcal{P}(\omega_3)$ below its expected value. These effects limit the sum-frequency power output and deserve a more detailed discussion.

IV. LIMITING PROCESSES

In their study of third harmonic generation in alkali vapors, Miles and Harris[24] have discussed various processes which limit the output power and the conversion efficiency. These processes include one photon absorption, multiphoton absorption and ionization, saturation, self-defocusing, and phase mismatch due to optical-field-induced refractive index. In the experiments described in the last section, several of these processes were important. In particular, the strong two-photon resonance and the one-photon near-resonant 3s → 3p transition in sum-frequency generation can lead to strong self-defocusing, saturation, and multiphoton ionization under certain conditions. We discuss these observations separately in the present section.

A. Linear Absorption

The linear absorption cross section for atomic sodium can be calculated from the data given by Miles and Harris.[24] In the density range we investigated, pressure broadening dominates the linewidth, and for $\Delta\omega_1 = (\omega_{3p_{\frac{1}{2}}} - \omega_1)$ and $\Delta\omega_1' = (\omega_{3p_{3/2}} - \omega_1)$ much larger than the linewidth, the absorption cross section is

$$\sigma \cong \frac{2\, r_e\, f\, \delta\nu_s (N/N_0)}{D^2} \tag{38}$$

where $r_e = 2.818 \times 10^{-13}$ cm, f is the oscillator strength of the D lines and is .982, $\delta\nu_s$ is the pressure broadening coefficient in cm^{-1}, and for the 3s - 3p transition has the value 42.7, N is the atomic density, and

$N_0 = 2.69 \times 10^{19}/cm^3$. D is an average frequency denominator given by

$$\frac{1}{D^2} \equiv \frac{1}{3}\frac{1}{\Delta\omega_1^2} + \frac{2}{3}\frac{1}{\Delta\omega_1'^2} \tag{39}$$

where the frequencies are in cm^{-1}. The sum-frequency output power $\mathcal{P}(\omega_3)$ is proportional to $N^2\mathcal{P}(\omega_1)\mathcal{P}(\omega_2)$ where $\mathcal{P}(\omega_1)$ and $\mathcal{P}(\omega_2)$ are the average pump beam powers in the nonlinear interaction region. For an interaction length less than 1 cm, the variation of the pump powers over the interaction length is negligible. Assuming the pump beams traverse a distance L in the atomic vapor before they overlap and assuming only absorption at ω_1 is appreciable, we then have

$$\begin{aligned} \mathcal{P}(\omega_1) &\propto \exp(-N\sigma L) = \exp(-\alpha N^2) \\ \mathcal{P}(\omega_3) &\propto N^2\exp(-\alpha N^2) \end{aligned} \tag{40}$$

where $\alpha = \sigma L/N$ is independent of N. The maximum output should therefore occur at

$$N_{opt} = \sqrt{1/\alpha} = \left(\frac{N_0 D^2}{2 r_e f \delta\nu_s L}\right)^{1/2}. \tag{41}$$

Since $L \approx 5$ cm in our case, our N_{opt} should be 4.77×10^{14} D. In Fig. 8 we show the observed variation of $\mathcal{P}(\omega_3)$ with density. For $\Delta\omega_1 = 40.8\ cm^{-1}$ and $\Delta\omega_1' = 58\ cm^{-1}$, $D = 50.1\ cm^{-1}$, so we expect the maximum QSFG to occur at $2.39 \times 10^{16}/cm^3$ in fair agreement with the observed value of $2.5 \times 10^{16}/cm^3$. For $\Delta\omega_1 = 80.4\ cm^{-1}$ and $\Delta\omega_1' = 97.6\ cm^{-1}$, $D = 90.7\ cm^{-1}$ and the

expected maximum is at $4.33 \times 10^{16}/cm^3$ while the observed maxiumum is at $5 \times 10^{16}/cm^3$. Since the vapor path is not accurately known, the agreement in both cases seems reasonable, and we conclude that atomic absorption limits the vapor density which can be used in our experiment. Dimer absorption was found to be much less important.

B. Saturation of Two-Photon Absorption

As is well known, when the intensities of the pump fields are sufficiently large, even two-photon absorption can be saturated. This has been observed in Cs vapor[28] and in Thallium vapor.[29]

As shown in Eq. (14), the third-order susceptibility for our quadrupole sum-frequency generation involving the 3s and 4d states is

$$\chi^{(Q)}_{M\alpha\beta} = (N\Delta\rho\langle 3s|q_M|4d\rangle/2\Delta\omega_2)\sum_p \frac{\langle 4d|p_\alpha|p\rangle\langle p|p_\beta|3s\rangle}{\hbar^2(\omega_p - \omega_1)} \qquad (42)$$

where $\Delta\rho \equiv (\rho_{3s} - \rho_{4d})$ and $\Delta\omega_2 \equiv \omega_{4d} - \omega_1 - \omega_2 - i\gamma$. The optical Stark shifts of all states are negligible in our case. Saturation comes in through the dependence of $\Delta\rho$ on the pump field intensities:[30]

$$\Delta\rho = \frac{\Delta\rho^0}{1 + W_{TP}T_1} \qquad (43)$$

where $\Delta\rho^0$ is the population difference at thermal equilibrium, W_{TP} is the two-photon transition rate and T_1 is a relaxation time for the population in $\langle 4d|$. If only radiative decay is considered, a value $T_1 = 1.1 \times 10^{-7}$ sec can be derived from tabulated transition probabilities.[31] The rate W_{TP} for cross polarized beams takes the form

$$W_{TP} = 2 \cdot \Omega^2(\gamma/|\Delta\omega_2|^2) \qquad (44)$$

with

$$\Omega^2 = \left| \sum_p \frac{\langle 4d|p_z|p\rangle\langle p|p_y|3s\rangle E(\omega_1)E(\omega_2)}{\hbar^2(\omega_p - \omega_1)} \right|^2 \tag{45}$$

denoting the two-photon Rabi frequency.[30,32] The square of the induced quadrupole moment density is given by

$$|Q_M|^2 = |\chi_M^Q : E(\omega_1)E(\omega_2)|^2 = (\Delta\rho^0)^2 |\langle 3s|q_M|4d\rangle|^2 \frac{N^2\Omega^2|\Delta\omega_2|^2}{\left[|\Delta\omega_2|^2 + 2\gamma\,\Omega^2\,T_1\right]^2} . \tag{46}$$

If the pump beams have Gaussian profiles, then Ω^2 also has a Gaussian profile. It can be shown that, for the unsaturated case at exact phase matching, the output power is

$$\mathcal{P}(\omega_3) \propto \int |Q|^2 \, d^3r. \tag{47}$$

This relation should hold approximately for the weakly saturated case ($2\gamma T_1\Omega^2 \lesssim \gamma^2$) with small induced index changes. We then find

$$\mathcal{P}(\omega_3) \propto \frac{\beta^2}{|\Delta\omega_2|^2} \int_{-\infty}^{\infty} \frac{e^{-y^2}\,dy}{\left[1 + (\beta^2\gamma^2/|\Delta\omega_2|^2)\exp(-y^2)\right]} \tag{48}$$

where $\beta^2 \equiv \frac{2T_1\Omega_0^2}{\gamma}$, and $\Omega_0 \equiv \Omega(r = 0)$.

In our experiment studying two-photon saturation effects on sum-frequency generation, we varied both laser intensities by using pairs of Glan-Thomson polarizers as attenuators. We fixed ω_1 at $\Delta\omega_1 = +41.2\ \text{cm}^{-1}$, and the vapor pressure at 0.4 torr. These values were chosen to make the self-defocusing effect negligibly small (see the following section). The frequency ω_2 was then varied to $\omega_1 + \omega_2$ over the two-photon resonance and

the peak output power and the resonant linewidth were recorded as functions of the product of the incident intensities. The results are shown in Fig. 9, together with theoretical curves obtained numerically from Eq. (48), using the parameter $\beta^2 = (7.6 \times 10^{-25}) I_1 I_2 (\text{esu})$. The data on peak output power agree well with the calculated curve. The data on resonant linewidths have large errors due to laser fluctuations but show an increase with $I_1 I_2$ in agreement with the predicted variation. The fact that defocusing was negligible in the experiment was confirmed by the result that $\mathcal{A}(\omega_3)$ is symmetric with respect to I_1 and I_2, since otherwise the difference in the self-defocusing strength of the two pump beams would introduce an asymmetry in the results. The parameter β^2 can be estimated theoretically from Eq. (48) using $T_1 = 1.1 \times 10^{-7}$ sec, $\gamma = 4.7 \times 10^{10}$/sec (taken as the sum of the laser linewidths), and

$$\frac{\Omega_0^2}{I_1 I_2} = \left(\frac{e a_0}{\hbar c}\right)^4 \frac{3}{4} \cdot z_{dp}^2 z_{ps}^2 \cdot \left(\frac{1}{\sqrt{3}\,\Delta\omega_1} + \sqrt{\frac{2}{3}} \frac{1}{\Delta\omega_1'}\right)^2 \qquad (49)$$

where $|z_{dp}| \equiv \langle 4d|z|3p\rangle$ and $|z_{ps}| = \langle 3p|z|3s\rangle$ taken from Ref. 24 are .864 and 2.51 respectively, $\Delta\omega_1 = +41.2\ \text{cm}^{-1}$ and $\Delta\omega_1' = +58.4\ \text{cm}^{-1}$. We find $\beta^2_{\text{theo.}} = (5.42 \times 10^{-25}) I_1 I_2$ esu. Since there are large errors in absolute intensities used in Eq. (49) , the agreement with the experimentally deduced value of $(7.6 \times 10^{-25}\ I_1 I_2)$esu should be considered satisfactory.

C. Induced Refractive Index Changes and Self-Defocusing

High pump intensities can induce refractive index changes in an atomic vapor through saturation of the dispersion,[33] two-photon resonance,[34] and induced population redistribution. For $\omega \sim \omega_{3p}$, saturation of the 3s → 3p transition gives, to the lowest order, an induced refractive in-

dex[35]

$$\delta n(\omega) = -\,8\pi N\hbar\left(\frac{ea_0 z_{ps}}{\hbar}\right)^4\left(\frac{T_1}{T_2}\right)\left[\frac{1}{9\,\Delta\omega^3}+\frac{4}{9\,\Delta\omega'^3}\right]|\vec{E}(\omega)|^2 \qquad (50)$$

where $\Delta\omega \equiv \omega_{3p_{\frac{1}{2}}} - \omega$, $\Delta\omega' \equiv \omega_{3p_{3/2}} - \omega$, and T_1 and T_2 are longitudinal and transverse relaxation times, respectively. When $\omega_1 + \omega_2 \approx \omega_{4d}$, the two-photon resonant dispersion also leads to an induced refractive index

$$\delta n'(\omega_1) = 2\pi N\hbar\left(\frac{ea_0}{\hbar}\right)^4 z_{ps}^2 z_{pd}^2 \cdot \frac{3}{4} \cdot \frac{1}{\Delta\omega_2} \times \left[\frac{11}{18}\frac{1}{\Delta\omega_1'^2}+\frac{2}{18\,\Delta\omega_1\Delta\omega_1'}+\frac{5}{18\,\Delta\omega_1^2}\right]|\vec{E}(\omega_2)|^2 \qquad (51)$$

and a similar expression with $|E(\omega_2)|^2$ replaced by $|E(\omega_1)|^2$ for $\delta n'(\omega_2)$. We have neglected here higher order contribution to δn. For values typical of our experiment, $N = 10^{16}/cm^3$, $\Delta\omega_1 = 10\ cm^{-1}$, $I(\omega_1) = I(\omega_2) = 10^5\ W/cm^2$, and $|\Delta\omega_2| = |(\omega_{4d} - \omega_1 - \omega_2 - i\Gamma)| \cong .25\ cm^{-1}$, we obtain $\delta n(\omega_1) = -\,1.13 \times 10^{-5}$, $|\delta n'(\omega_1)| = |\delta n'(\omega_2)| = 2 \times 10^{-6}$. It is seen that $\delta n'(\omega)$ is negligible compared with $\delta n(\omega_1)$. At exact two-photon resonance, $\delta n'(\omega)$ is purely imaginary, and corresponds to an absorption length of 2.3 cm.

The field induced refractive index can effect the generation of sum-frequency by self-defocusing of the pump beams[36,37] and by destroying the phase matching. Consider self-defocusing first. In the paraxial approximation[38] the beam radius σ changes as the beam propagates according to

$$\frac{\sigma^2(z)}{\sigma^2(0)} = z^2/R_{eff}^2 + 2z/R + 1$$

$$R_{eff}^{-2} \equiv R^{-2} + R_d^{-2} + R_{NL}^{-2} \qquad (52)$$

where z is the distance travelled through the medium, R is the radius of curvature of the wavefront at z = 0 (R < 0 for a focused beam), $R_d = 2k\sigma^2(0)$ is the diffraction length, $R_{NL}^2 = - n_0^2\sigma^2(0)/4\delta n^0$ is the non-linear diffraction length, with δn^0 and n_0 the induced refractive index on the beam axis at z = 0, and the background index respectively. Then, the ratio of the two beam radii with and without self-defocusing is

$$\frac{\sigma(z)}{\sigma^0(z)} = [1 + C(z)|\delta n^0|]^{\frac{1}{2}}$$
$$C^{-1}(z) \equiv (n_0^2\sigma^2(0)/4)(z^{-2} + 2(Rz)^{-1} + R_d^{-2} + R^{-2}). \tag{53}$$

Self-defocusing of the beams may affect the sum-frequency power output.

As seen from Eq. (34), we have

$$\mathcal{P}_{out}(\omega) \propto F \cong 2/(\sigma_1/\sigma_2 + \sigma_2/\sigma_1) \tag{54}$$

where σ_1/σ_2 is the ratio of the two pump beam radii in the intersection region. In our case, only self-defocusing of the ω_1 beam was appreciable. To estimate its importance we found from measurements that in our experimental case, $C(z) \cong 2 \times 10^5$ in the beam intersection region. Then, with $\delta n^0 = - 10^{-5}$ the output will be reduced by 25%. For strong self-defocusing with $\sigma_1(z) >> \sigma_1^0(z)$, $\sigma_2(z)$ in the beam intersection region, the output power $\mathcal{P}(\omega)$ becomes proportional to $\mathcal{P}(\omega_2)\mathcal{P}(\omega_1)^{\frac{1}{2}}$ rather than $\mathcal{P}(\omega_2)\mathcal{P}(\omega_1)$, as can be seen from Eqs. (53) and (54).

Possibly a more devastating effect of δn is the breaking of phase matching. Let us assume that for phase matching with $\delta n = 0$, the angles the pump beams make with $\hat{z}$ are θ_{1p} and θ_{2p}. The induced $\delta n_i \equiv \delta n(\omega_i)$

change the $\vec{k}$ vectors so that $\Delta\vec{k} \neq 0$, and the output power of Eq. (33) becomes

$$\mathcal{P}(\omega_3) \propto \exp\left\{ - \frac{[(\delta n_3 - \delta n_1 \cos\theta_{1p})\omega_1 + (\delta n_3 - \delta n_2 \cos\theta_{2p})\omega_2]^2}{(\sigma_1^{-2}\sin^2\theta_{1p} + \sigma_2^{-2}\sin^2\theta_{2p})c^2} \right\} . \quad (55)$$

Since in our case $\delta n_2 \approx \delta n_3 \approx 0$, using $k_1 \sin\theta_{1p} = k_2 \sin\theta_{2p}$ we find

$$\mathcal{P}(\omega_3) \propto \exp\left\{ \frac{-\delta n_1^2}{n_1^2 \tan^2\theta_{1p}(\sigma_1^{-2} k_1^{-2} + \sigma_2^{-2} k_2^{-2})} \right\} . \quad (56)$$

If $n_1 \approx 1$, $\omega_1 \approx \omega_2$ and $\sigma_1 \approx \sigma_2$, the denominator in the exponential is $(2\theta_{1p}^2 k_1^{-2} \sigma_1^{-2})$. For our experiment this is about $(1.8 \times 10^{-5})^2$. Thus, a value $\delta n = 10^{-5}$ will reduce the output power by 27%. At larger δn, because the factor in Eq. (55) is a Gaussian, the induced phase mismatch cuts off the output power much more sharply than self-defocusing.

We now want to obtain some estimate of $\delta n(\omega_1)$ and its effect on sum-frequency generation under our experimental conditions. In order to deduce $\delta n(\omega_1)$, we measured the self-defocusing of the beam at $\omega_1 \simeq \omega_{3p}$. The experimental arrangement is shown in Fig. 10. Let θ_B and θ^0 be the full divergence angles of the beam at ω_1 with and without self-defocusing respectively. Then we have $(\theta_B/\theta^0)^2$ inversely proportional to the ratio of powers transmitted through the pinhole (diameter = 0.5 mm) with and without self-defocusing. From Eq. (52) we find

$$\theta_B^2 = 4\sigma^2(0)/R_{eff}^2$$

$$= (\theta^0)^2 - \frac{16\,\delta n^0}{n_0^2} \quad (57)$$

where $(\theta^0)^2 = 4\sigma^2(0)(R^{-2} + R_d^{-2})$. We can then obtain δn^0 from the measured θ^0 and θ_B. For our focused laser beam, we had $(n_0\theta^0/4)^2 = 2.25 \times 10^{-6}$.

The results of our self-defocusing measurement are shown in Fig. 11. The curve of Fig. (11a) shows the measured values of $[(\theta_B/\theta^0)^2 - 1]$, which according to Eq. (57) is proportional to $\delta n^0(\omega_1)$, as a function of $\Delta\omega_1$. The defocusing increases sharply for small detunings. The solid curve was calculated, aside from a proportional factor, from Eq. (50), with $|E(\omega_1)|^2 = |E_0(\omega_1)|^2 \exp(-\alpha\ell)$, where E_0 is the field in the beam intersection region in the absence of absorption, α is the absorption coefficient, and ℓ is the distance from the vapor boundary to the beam intersection region. The magnitude of $\delta n^0(\omega_1)$ deduced from the experimental result of $(\theta_B/\theta^0)^2$ at $\Delta\omega_1 = 14.9$ cm^{-1} for example is $\delta n = 4.5 \times 10^{-5}$. This is in rough agreement with $\delta n = 1.3 \times 10^{-5}$ calculated from Eq. (50).

The curves of Fig. (11b) show the results of simultaneous measurements of self-defocusing and sum-frequency power output. As the ω_1-beam begins to self-defocus, the output starts to fall. To assess the relative importance of self-defocusing, induced phase mismatch, and two-photon resonant saturation, we consider the case with $\Delta\omega_1 = 41.2$ cm^{-1}, $I(\omega_1) = 4.6 \times 10^5$ W/cm^2, and $I(\omega_2) = 5.5 \times 10^4$ W/cm^2. The experimental measurement of self-defocusing gives $\delta n(\omega_1) \cong 1.5 \times 10^{-5}$. In this case, the effects of self-defocusing, induced phase mismatch, and saturation on $\mathcal{G}(\omega)$ are comparable. Using Eqs. (53), (54), and (56), and Eq. (48), we estimate the reductions of $\mathcal{P}(\omega)$ due to the three mechanisms are 0.8, 0.5, and 0.5 respectively. The total reduction of $\mathcal{P}(\omega)$ is roughly in agreement with that observed. For larger values of δn, the effect of

induced phase mismatch begins to dominate. While self-defocusing and saturation would at worst cause $\mathcal{P}(\omega)$ to decrease slowly with $\mathcal{P}(\omega_1)$, the induced phase-mismatch could cause $\mathcal{P}(\omega)$ to decrease sharply with increase of $\mathcal{P}(\omega_1)$. This was actually observed in our experiment. When the induced phase mismatch is important, the phase-matching curve is appreciably broadened, as was also observed. We notice that in order to avoid the detrimental effects on $\mathcal{P}(\omega)$, we must have $\delta n \lesssim 10^{-5}$. This a fairly stringent requirement. It limits the laser intensity $I(\omega_1)$ to $\sim 10^6$ W/cm^2 even for $\Delta\omega_1 = 40$ cm^{-1} at a pressure of 2 torr. Induced refractive index change is therefore the strongest limiting factor for sum-frequency generation in our experiment.

D. Multiphoton Ionization

Multiphoton ionization also plays an important limiting role in near-resonant nonlinear processes. Miles and Harris[24] suggest that it may be the dominant process limiting allowable incident power, and the recent report[39] of nearly complete photoionization of a sodium vapor by a single dye laser pulse emphasizes its importance. Teague and Lambropolous[40] have recently calculated three-photon ionization cross sections for sodium under near-resonant conditions. For a laser frequency 11 cm^{-1} below the $3s \rightarrow 3p_{\frac{1}{2}}$ transition, their calculated cross section is $\sigma^{(3)} = 2.38 \times 10^{-75}$ cm^6 sec^2. For our laser intensity $I(\omega_1)$(1 MW/cm^2 $\sim 3 \times 10^{24}$/cm^2 sec) this gives an ionization rate 6.2×10^{-2}/sec, or for a laser pulsewidth of 500 ns, an ionization probability 3.1×10^{-8}/atom. In the absence of an applied electric field and avalanche breakdown, this ionization level would not have much effect. However, the ionization cross section increases dramatically when a second laser beam is present with $\omega_1 + \omega_2 \cong$

ω_{4d}. For $\omega_1 + \omega_2 - \omega_{4d} = 0.5\ cm^{-1}$, and $\Delta\omega_1 = +11\ cm^{-1}$, Teague and Lambropoulos estimated an ionization cross section $\sigma^{(3)} = 4.15 \times 10^{-69}\ cm^6\ sec^2$. With $I(\omega_1) = I(\omega_2) = 1\ MW/cm^2$, the corresponding ionization rate is $\sigma^{(3)} I_1 I_2 (I_1 + I_2) = 2.16 \times 10^5/sec$, giving a fractional ionization of $\sim 10\%$. In our experiments, we have not measured the ionization rate directly. However, from current induced between two electrodes in the cell, it seems quite certain that fractional ionizations above one per cent were present at the highest intensity levels used ($I_1 \sim I_2 \sim .5\ MW/cm^2$) with $\omega_1 + \omega_2 = \omega_{4d}$ and $\Delta\omega_1 = 10\ cm^{-1}$.

V. MEASUREMENT OF A QUADRUPOLE TRANSITION MOMENT BY INTERFERENCE OF QUADRUPOLE AND DC-FIELD-INDUCED SUM-FREQUENCY GENERATION

A. Introduction

In recent years, there have been a number of calculations of atomic quadrupole transition moments.[25,41-43] The corresponding experimental work is however extremely rare. Bogaard and Orr[42] have proposed measuring the quadrupole moments by observing the field-induced birefringence of an atomic vapor in a strong electric field gradient, but concluded the effect is much too small to allow a decent signal-to-noise ratio. Lambropoulous et al.[44] have reported the observation of a multiphoton ionization process involving a quadrupole transition. By comparing the ionization rate of the (3s → 3p → 4f → continuum) process with that of the (3s → 3p → 4d → continuum) process, they were able to deduce the 3p → 4f quadrupole moment. The accuracy, however, depends critically on the dipole matrix elements of 3p → 4d, 4d → continuum, and 4f → continuum. We have found that it is possible to use a nonlinear optical technique to measure quadrupole transition moments relative to the known dipole matrix elements. The technique is based on the interference between quadrupole[45] and dc-field-induced[46] sum-frequency generation. It gives not only the magnitude but also the sign of the quadrupole matrix elements and has an inherently high accuracy. A similar method based on the interference between magnetic-dipole and dc-field-induced dipole transitions in single-photon absorption has been used to measure the magnetic-dipole matrix elements in atomic vapors.[47] As a preliminary example, we have measured 3s → 4d quadrupole moment of sodium.

B. Theory

Let $\vec{E}_1$ at ω_1 and $\vec{E}_2$ at ω_2 be the incoming pump fields. The nonlinear polarization $\vec{P}^{NL}$ responsible for the sum-frequency generation at $\omega_3 = \omega_1 + \omega_2$ near q quadrupole resonance is given by[45]

$$\vec{P}^{NL}(\omega_3) = \left[- i\vec{k}_3 \cdot \overleftrightarrow{\chi}_Q^{(2)} + \overleftrightarrow{\chi}^{(3)} \cdot \vec{E}_0 \right] : \vec{E}_1\vec{E}_2 \qquad (58)$$

where $\vec{E}_0$ is the applied dc field, $\overleftrightarrow{\chi}_Q^{(2)}$ is the quadrupole second-order nonlinear susceptibility, and $\overleftrightarrow{\chi}^{(3)}$ is the third-order nonlinear susceptibility. Since the sum-frequency signal is proportional to $|\vec{P}^{NL}(\omega_3)|^2$, variation of the sum-frequency signal resulting from variation of E_0 should yield a value for the ratio $\chi_Q^{(2)}/\chi^{(3)}$, from which the particular quadrupole matrix element can be deduced in terms of dipole matrix elements.

More specifically, consider the case of sodium vapor with ω_1 close to ω_{3p} and $\omega_1 + \omega_2$ resonant with ω_{4d}. Insertion of the microscopic expressions for $\overleftrightarrow{\chi}_Q^{(2)}$ and $\overleftrightarrow{\chi}^{(3)}$ in Eq. (58) leads to

$$\vec{P}^{NL}(\omega_3) \cong \frac{Ne^3}{\hbar^2} \left[- i\vec{k}_3 \cdot \overleftrightarrow{M}_Q + \overleftrightarrow{M}_D \cdot \vec{E}_0 \right] \times \frac{\langle 4d|\vec{r}|3p\rangle\langle 3p|\vec{r}|3s\rangle : \vec{E}_1\vec{E}_2}{(\omega_1 - \omega_{3p})(\omega_3 - \omega_{4d} + i\Gamma)}$$

where $\overleftrightarrow{M}_Q = \langle 3s|\tfrac{1}{2}\,\vec{r}\,\vec{r}|4d\rangle$ and

$$\overleftrightarrow{M}_D = e \sum_{np} \left\{ \frac{-\langle 3s|\vec{r}|np\rangle\langle np|\vec{r}|4d\rangle}{\hbar(\omega_3 - \omega_{np})} + \frac{\langle np|\vec{r}|4d\rangle\langle 3s|\vec{r}|np\rangle}{\hbar\omega_{np}} \right\}. \qquad (59)$$

If we use the noncollinear geometry for sum-frequency generation shown in Fig. 12 with $\vec{k}_1$ and $\vec{k}_2$ in the $\hat{x} - \hat{z}$ plane, $\vec{k}_3$ along $\hat{z}$, $\vec{E}_0$ and $\vec{E}_1$ along $\hat{y}$, and $\vec{E}_2 = (\hat{x}\cos\theta_2 + \hat{z}\sin\theta_2)E_{2h} + \hat{y}\,E_{2y}$, then from symmetry arguments, we can write

$$P_x^{NL}(\omega_3) = (M_D)_{xy} F_{yx} E_0 E_1 E_{2h} \cos\theta_2$$

$$P_y^{NL}(\omega_3) = \left[- ik_3 (M_Q)_{yz} F_{yz} \sin\theta_2 + (M_D)_{yy} F_{yy} E_0 (E_{2y}/E_{2h}) \right] E_1 E_{2h} \tag{60}$$

where

$$F_{yx} = \frac{Ne^3}{\hbar^2} \frac{\langle 4d|y|3p\rangle\langle 3p|x|3s\rangle}{(\omega_1 - \omega_{3p})(\omega_3 - \omega_{4d} + i\Gamma)}$$

$$= F_{yz} = (\sqrt{3}/2) F_{yy} = (\sqrt{3}/2) F_{zz} \tag{61}$$

$$(M_D)_{zz} = (M_D)_{yy} = (2/\sqrt{3})(M_D)_{xy} \ , \ (M_Q)_{zz} = (2/\sqrt{3})(M_Q)_{yz}.$$

The sum-frequency field $\vec{E}_3(\omega_3)$ is now directly proportional to $\left[\hat{x} P_x^{NL}(\omega_3) + \hat{y} P_y^{NL}(\omega_3) \right]$. Thus, if $\vec{E}_2$ is circularly polarized so that $E_{2y}/E_{2h} = \pm i$, then the $\hat{y}$ component of the output $\vec{E}_3(\omega_3)$ will vanish when

$$E_0 = \pm (3/4) k_3 (M_Q)_{zz} \sin\theta_2 / (M_D)_{zz}. \tag{62}$$

If $\vec{E}_2$ is linearly polarized in the $\hat{x}$ - $\hat{z}$ plane, then the output $\vec{E}_3$ becomes circularly polarized when

$$E_0 = \pm k_3 (M_Q)_{zz} \tan\theta_2 / (M_D)_{zz}. \tag{63}$$

In either case, from the measured value of E_0, we can deduce the ratio $(M_Q)_{zz}/(M_D)_{zz}$ including the sign.

C. Experiment

1. Experimental Set-Up

As an application of the technique described above, we have measured the quadrupole transition moment $\langle 3s|\frac{1}{2}zz|4d\rangle$ of sodium which enters the QSFG experiment described earlier.

In order to apply a transverse electric field, a pair of stainless steel electrodes were inserted into the heat pipe. The electrodes themselves were flat plates ~ 1.8 cm × 3.8 cm × 0.3 cm, separated by 0.095 ± .005 cm, with all edges and corners rounded. Each was supported by two Alumina rods which seated in round grooves along the long edges of the plate. To avoid condensation of sodium on the plates and eventual shorting, two-hole bored Alumina rods were used, and nichrome wire was threaded through the rods, allowing them to be heated above the wall temperature of the heat pipe.

The dc field was applied in a 10 μsec square pulse, synchronized to the 0.5 μsec dye laser pulses at ω_1 = 16900 cm^{-1} and ω_2 = 17649 cm^{-1}. We operated the heat pipe at a vapor pressure of 1 torr. When ω_1 was tuned ~ 10 cm^{-1} below $\omega_{3p_{\frac{1}{2}}}$ and $\mathcal{P}(\omega_1)$ ~ 100 W, even with no input at ω_2 an ionization current of approximately 1 Amp peak current was measured with ~ 50 V applied across the plates. The current rose sharply, synchronous with the laser pulse, and decayed more slowly, with an apparent decay time of several microseconds. In order to avoid this heavy ionization of Na by resonant three photon ionization processes, we limited the peak laser power at ω_1 to ~ 10 watts and that at ω_2 to ~ 100 watts and tuned ω_1 quite far (56 cm^{-1}) from $\omega_{3p_{\frac{1}{2}}}$. At these power levels, ionization of Na was less than 1% as judged from the induced current between the two electrodes. However, with the angle between $\vec{k}_1$ and $\vec{k}_2$ adjusted

to phase matching for sum-frequency generation ($\theta_1 \cong \theta_2 = 13$ mrad), the output signal at $E_0 = 0$ still had a peak power of ~ 1 μW and could easily be detected.

2. Results

Our results with $\vec{E}_2$ linearly polarized in the $\hat{x} - \hat{y}$ plane are shown in Fig. 13 as $I_x(\omega_3)/I_y(\omega_3)$ versus E_0, where $I_x(\omega_3)$ and $I_y(\omega_3)$ are the sum-frequency output intensities polarized along $\hat{x}$ and $\hat{y}$ respectively. Following Eq. (60), we should have

$$I_x(\omega_3)/I_y(\omega_3) = \left|(M_D)_{zz}\, E_0/k_3(M_Q)_{zz} \tan\theta_2\right|^2 \qquad (64)$$

which becomes unity when E_0 satisfies Eq. (63). When $I_x/I_y = 1$, the output should be circularly polarized. We found experimentally that this was indeed the case since the output transmitted through a linear uv polarizer was then independent of analyzer rotation angle to within 10%. In the absence of a uv circular polarizer, we did not analyze the handedness of the circular polarization. Using Eq. (64) to fit the data points in Fig. 13, we obtained $\left|(M_Q)_{zz}/(M_D)_{zz}\right| = (4.4 \pm 0.4) \times 10^{-4}$ statvolts. The uncertainty was mainly due to laser power fluctuations.

We also used a Polaroid circular polarizing sheet to left circularly polarize $\vec{E}_2$, so that $E_{2y}/E_{2h} \approx +i$, and measured $I_y(\omega_3)$ as a function of E_0. The results are shown in Fig. 14. According to Eq. (60), we should have

$$I_y(\omega_3) \propto \left|(3/4)k_3(M_Q)_{zz} \sin\theta_2/(M_D)_{zz} - E_0\right|^2. \qquad (65)$$

As E_0 increases to positive values from 0, $I_y(\omega_3)$ should first decrease

if $(M_Q)_{zz}/(M_D)_{zz}$ is positive. This was the case we found experimentally. Since the circular polarizer we used was not perfect, we did not have $I_y(\omega_3)$ go exactly to zero at a certain value of E_0 as predicted by Eq. (65), but if we assume E_0 of Eq. (62) corresponds to the observed minimum of $I_y(\omega_3)$, then we could deduce from the experimental data $(M_Q)_{zz}/(M_D)_{zz} = + (4.45 \pm 0.8) \times 10^{-4}$ statvolt, which is very close the value derived earlier in the measurement with linear polarizations.

We can now find the quadrupole transition moment $(M_Q)_{zz} = \langle 3s|\tfrac{1}{2} zz|4d\rangle$ of sodium if $(M_D)_{zz}$ is known. The latter can actually be calculated from the tabulated transition frequencies and dipole matrix elements for sodium.[24] According to Ref. 24, all dipole matrix elements between 3s and np and between np and 4d with n = 3, 4, 5, 6 are negative except $\langle 5p|z|4d\rangle$ which is positive. Using these matrix elements, we obtained from Eq. (59) $(M_D)_{zz} = + 5.1 \times 10^3\ a_0^2$/statvolt and hence $(M_Q)_{zz} = + 2.2\ a_0^2$, where a_0 is the Bohr radius. This is about 50% larger than the value[48] $|(M_Q)_{zz}| = 1.36$ a.u. calculated by Tull et al.[25] Aside from possible large uncertainty in the calculation, we do not know other causes for the discrepancy.

D. Discussion

The technique described here can of course be used to measure other $s \rightarrow d$ quadrupole transition moments. It can also be used to measure $p \rightarrow p$ quadrupole moments by observing interference between $s \rightarrow p \rightarrow p \rightarrow s$ quadrupole sum- (or difference-) frequency generation and $s \rightarrow p \rightarrow d \rightarrow p \rightarrow s$ or $s \rightarrow p \rightarrow s \rightarrow p \rightarrow s$ dc-field-induced sum- (or difference-) frequency generation.

The dc-field-induced sum-frequency generation is of some interest by

itself. Unlike the quadrupole case, the nonlinear susceptibility $\chi^{(3)}$ gives nonvanishing SFG for the collinear beam geometry. As a result, dc-field-induced sum-frequency generation with collinear phase matching is possible. The process is in fact more efficient than the quadrupole process at a dc field $E_0 \gtrsim 500$ v/cm. However, the efficiency of resonant optical mixing in metal vapor is always limited at high laser intensities by saturation, multiphoton ionization and self-defocusing. In order to improve the efficiency, the pump beams must be expanded. This requires greater electrode plate separation and higher voltage across the plates in the dc-field-induced case. Consequently, the problem of avalanche breakdown initiated by multiphoton ionization of atoms in the dc field becomes much more severe and may prevent the use of the dc-field-induced process for very efficient sum or difference frequency generation. The alternative of applying a transverse magnetic field as in the experiments of Flusberg et al.[17] avoids this problem and may give efficient collinear three wave mixing if phase matching can be achieved at reasonably high densities.

E. Conclusion

Our experiment confirms the possibility of using this nonlinear optical technique for measuring both the magnitude and the sign of atomic quadrupole transition moments relative to the dipole matrix elements. The technique is inherently very accurate. In the present work, it is limited by the pulsed laser power fluctuations. However, since the sum-frequency signal is far above noise, it is possible that stable CW dye lasers can be used for such measurements. The accuracy of the measurements can then be greatly improved.

VI. QUADRUPOLE PUMPED PROCESSES

We have so far considered the sum-frequency generation process in which mixing of two pump beams at ω_1 and ω_2 induces a quadrupole polarization at $\omega = \omega_1 + \omega_2$. As seen in the derivation of the generalized susceptibility of Eq. (9), we can also have an electric dipole polarization induced by mixing of two pump fields, one of which is coupled to a quadrupole transition. We can write, for example,

$$\vec{P}(\omega) = \overleftrightarrow{\chi}^{(Q_1)}(\omega = \omega_1 + \omega_2) : (i\vec{k}_1)\vec{E}_1(\omega_1)\vec{E}_2(\omega_2) \tag{66}$$

where $\vec{E}_1$ is coupled to a quadrupole transition. If ω_1 and ω_2 are both near quadrupole transitions, a second term with ω_1 and ω_2 permuted should be added to the sides of Eq. (66) and Eq. (68) below. For difference-frequency generation, we simply replace ω_2 by $-\omega_2$ and $\vec{E}_2$ by $\vec{E}_2^*$. At frequencies sufficiently far away from resonance so that damping is negligible, $\overleftrightarrow{\chi}^{(Q_1)}$ for the difference frequency $\omega = \omega_1 - \omega_2$ and $\overleftrightarrow{\chi}^{(Q)}$ for the sum frequency $\omega = \omega_1 + \omega_2$ discussed earlier are related through the permutation symmetry[50]

$$\chi^{(Q_1)}_{\alpha\beta\gamma\delta}(\omega_2 = \omega - \omega_1)^* = \chi^{(Q)}_{\beta\gamma\delta\alpha}(\omega = \omega_1 + \omega_2). \tag{67}$$

The microscopic expression for $\overleftrightarrow{\chi}^{(Q_1)}$ can therefore be obtained directly from that of $\overleftrightarrow{\chi}^{(Q)}$. At resonance, the microscopic expressions of the $\overleftrightarrow{\chi}^{(Q_1)}$ and $\overleftrightarrow{\chi}^{(Q)}$ should be modified to include the damping coefficients properly in the frequency denominators as discussed earlier in Sec. IIA for $\overleftrightarrow{\chi}^{(Q)}$. Using symmetry arguments, we can also write Eq. (66) in the form

$$\vec{P}(\omega) = i\, \chi^{(Q_1)}_{-1,2,-1}(\omega = \omega_1 + \omega_2)[\vec{E}_1(\vec{k}_1 \cdot \vec{E}_2) + \vec{k}_1(\vec{E}_1 \cdot \vec{E}_2)]. \quad (68)$$

As an example, we consider the possible case of quadrupole-pumped difference-frequency generation in Cs vapor. We assume two pump fields at ω_1 and ω_2 which are respectively at resonance with the 4s - 6d quadrupole transition with $\omega_{6d_{5/2}} = 22631.8\ \mathrm{cm}^{-1}$ and near resonance with the 4s - 7p transition with $\omega_{7p_{3/2}} = 21946.7\ \mathrm{cm}^{-1}$. The dominant term of $\chi^{(Q_1)}_{-1,2,-1}$ $(\omega = \omega_1 - \omega_2)$ for difference frequency generation at $\omega \sim 685\ \mathrm{cm}^{-1}$ is

$$\chi^{(Q_1)}_{-1,2,-1} \simeq \frac{Ne^3}{2\hbar^2} \frac{I^{6,7,6}_{sdps}}{15} \left(\frac{9}{15} \cdot \frac{1}{(\omega_{6d_{5/2}} - \omega_1)(\omega_{7p_{3/2}} - \omega_2)} \right). \quad (69)$$

To estimate $I^{6,7,6}_{sdps}$, we can use the tabulated radial integrals for Cs, and the conservative approximation $\langle 6s\| r^2 \| 6d\rangle_{Cs} \simeq \langle 3s\| r^2 \| 3d\rangle_{Na}$, the quadrupole radial matrix element of Na from Ref. 25. For $N = 10^{16}$, $\omega_{6d_{5/2}} - \omega_1 =$ $.25\ \mathrm{cm}^{-1}$, and $\omega_{7p_{3/2}} - \omega_2 = 2\ \mathrm{cm}^{-1}$, we obtain $\chi^{(Q_1)}_{-1,2,-1} = 2.1 \times 10^{-13}$ esu. This should yield an infrared output power $\mathcal{P}_{ir} = \mathcal{P}_1\mathcal{P}_2/1.5 \times 10^9$ W at $\sim$ $685\ \mathrm{cm}^{-1}$ (14.6 μm). For two 40 KW input beams the output power should be about 1 W.

VII. SUMMARY AND CONCLUSIONS

We have demonstrated that second-order sum-frequency generation is observable in isotropic media. The requirement that the medium lack inversion symmetry for second order nonlinear susceptibilities is replaced by a requirement that a tensor product of the input fields lack two-fold symmetry about the phase matching direction. This requires a noncollinear geometry.

The sum-frequency generation is described by a quadrupole susceptibility which gives the quadrupole moment density induced by two fields. The spherical symmetry of the atom allows us to define a scalar susceptibility, and derive the geometric structure of the atomic quadrupoles directly from the input field polarization vectors.

Since they are lower order in perturbation theory, dipole forbidden susceptibilities can have effective magnitudes comparable to third or higher order dipole allowed susceptibilities. For example, at resonance the sodium quadrupole susceptibility has magnitude 10^{-14} esu, or when multiplied by k, an effective dipole susceptibility of 10^{-9} esu, which is as large as $\chi^{(2)}$ in quartz. However, the noncollinear geometry gives a radiating transverse component of the effective dipole fifty times smaller. Our results emphasize the fact that laser sources make it possible to observe and exploit weak transitions, which until recently, could be safely neglected.

Application of a transverse magnetic field alters the relative strengths of interfering resonant contributions to the susceptibility, so that collinear QSFG becomes possible. Although the B-field induced susceptibility is reduced by the ratio of the Zeeman splitting to the

Doppler width, this is compensated by the nearly transverse effective dipole polarization, so the B-field induced and non-B-field induced signals may be comparable for a field of ~ 10 Gauss.

Our experiments in Na vapor on QSFG showed the very sharp two-photon resonance enhancement and phase matching characteristics expected from theory, and verified the dependence of the output power on several other parameters. Deviations from the simple theory at higher intensities and densities, or small detunings from the intermediate state can be satisfactorily accounted for by the effects of 1) linear absorption associated with the D-line resonances (which also give the dispersion necessary for noncollinear phase matching); 2) saturation of the two-photon 3s → 4d transition; and 3) loss of phase matching due to induced index of refraction changes in the vapor. By expanding the input beams the last two effects may be circumvented, at the price of making the phase matching more critical, and requiring very low divergence input beams.

We have also shown that by applying a D.C. electric field to the vapor, the D.C. induced third-order sum frequency light interferes with the QSFG, allowing the quadrupole transition moment to be measured relative to the dipole matrix elements of the atom. In this way we have measured the 3s → 4d quadrupole moment of Na. This technique should allow accurate determination of both electric quadrupole and magnetic-dipole transition moments.

Finally we have described the extension of dipole forbidden susceptibilities to the case of difference frequency generation in Cesium, with direct pumping of a quadrupole transition resulting in a dipole allowed output radiation as a possible source of 12-14 μ radiation.

This work is supported by the U.S. Energy Research and Development

Administration.

APPENDIX A: EFFECT OF DOPPLER BROADENING AND LASER LINEWIDTH ON TWO-PHOTON RESONANT QSFG

If we assume the atoms of the vapor have velocities distributed according to the Maxwell distribution $V(\vec{v})$, which we take to be normalized, the dispersion functions $A_{jj'}^{nn'}$ and $B_{jj'}^{nn'}$ in Eq. (21) must be replaced by a sum of contributions from different velocity groups. For atoms with velocity $\vec{v}$, the laser frequencies are shifted in first order to $(\omega_1 - \vec{k}_1 \cdot \vec{v})$ and $(\omega_2 - \vec{k}_2 \cdot \vec{v})$. The dispersion functions become

$$A_{jj'}^{nn'} = \int V(\vec{v}) d^3\vec{v} \left\{ \frac{1}{D_{nd_j}(\omega - \vec{k} \cdot \vec{v}) D_{n'p_{j'}}(\omega_1 - \vec{k}_1 \cdot \vec{v})} + \frac{1}{D_{nd_j}(-\omega + \vec{k} \cdot \vec{v}) D_{n'p_{j'}}(-\omega_1 + \vec{k}_1 \cdot \vec{v})} \right\} \tag{A1}$$

$$B_{jj'}^{nn'} = \int V(\vec{v}) d^3\vec{v} \left\{ \frac{1}{D_{np_j}(-\omega_2 + \vec{k}_2 \cdot \vec{v}) D_{n'p_{j'}}(\omega_1 - \vec{k}_1 \cdot \vec{v})} \right\}$$

where we have set $\omega_1 + \omega_2 = \omega$ and $\vec{k}_1 + \vec{k}_2 = \vec{k}$. In this appendix we consider the case where $\omega \simeq \omega_{nd}$, while all other terms are far enough off resonance to be unaffected by Doppler broadening or finite laser linewidth. We concentrate on the first term of (A1) and suppress the principal quantum numbers. With the collision broadened width $\gamma_{nd_j} \equiv \gamma$ inserted, we have

$$A_{jj'} = \int \frac{V(\vec{v}) d^3\vec{v}}{(\omega_{d_j} - \omega + \vec{k} \cdot \vec{v} - i\gamma)(\omega_{p_{j'}} - \omega_1 + \vec{k}_1 \cdot \vec{v})} . \tag{A2}$$

With the assumption $k_1 v << \omega_{p_{j'}} - \omega_{L_1}$ where ω_{L_1} is the center frequency of laser 1, the second factor in the denominator can be set to its v = 0

value and removed from the integral. Then, with $\vec{k} \parallel \hat{z}$, the v_x and v_y integrations are trivial and, with $v_z \equiv v$,

$$A_{jj'} = \frac{h}{(\omega_{p_{j'}} - \omega_1)} \int_{-\infty}^{\infty} \frac{dv\ e^{-(v^2/2mk_BT)}}{(\omega_{d_j} - \omega + kv - i\gamma)} = \frac{Z(\Delta_j + i\Gamma)}{(\omega_{p_{j'}} - \omega_1)\Omega} \tag{A3}$$

where $h = \sqrt{m/2\pi k_B T}$, Z is the plasma dispersion function[50]

$$Z(x + iy) \equiv \pi^{-\frac{1}{2}} \int_{-\infty}^{\infty} dt\ \exp(-t^2)/(t - x - iy), \tag{A4}$$

$\Omega = \omega\sqrt{2k_BT/mc^2}$ is the sum-frequency Doppler width, and $\Delta_j + i\Gamma = (\omega - \omega_j + i\gamma)/\Omega$. If several ω_j values are near two photon resonance and/or a magnetic field splits the state into Zeeman sublevels, we must sum over these levels according to Eq. (14), with weighting factors derived from the products of Clebsch-Gordan and Racah coefficients which arise when the matrix elements are evaluated. We call these weighting factors $W^{m\alpha\beta}_{jj'm}$, where j and j' are the total angular momenta in the d and p states, and $m = \pm \frac{1}{2}$ is the ground state z spin component. The m_j values in the d and p states are fixed by $m_{j_p} = m + \beta$, $m_{j_d} = m - M$. The total dispersion function in the near resonant case is then given by

$$A_{M\alpha\beta}(\omega,\omega_2,\omega_1) = \sum_{jj'm} W^{M\alpha\beta}_{jj'm} \frac{Z(\Delta_{jm} + i\Gamma)}{(\omega_{p_{j'}} - \omega_1)\Omega}$$

$$\chi^{(Q)}_{M\alpha\beta}(\text{Doppler}) = G\, A_{M\alpha\beta}(\omega,\omega_2,\omega_1). \tag{A5}$$

The induced quadrupole moment will have time dependence

$$Q_M(t) = G \int_{-\infty}^{\infty} \int_{-\infty}^{\infty} e^{-i\omega t} A_{M\alpha\beta}(\omega,\omega_2,\omega_1) E_\alpha(\omega_2) E_\beta(\omega_1) d\omega_2 d\omega_1 \qquad \text{(A6)}$$

with the Fourier transform

$$Q_M(\omega) = G \int_{-\infty}^{\infty} A_{M\alpha\beta}(\omega,\omega-\omega_1,\omega_1) E_\alpha(\omega-\omega_1) E_\beta(\omega_1) d\omega_1. \qquad \text{(A7)}$$

G is a constant = $(Ne^3/2\hbar^2)(I^{nn'n''}/15)$. For our case, the intermediate state detuning, $(\omega_{p_j'} - \omega_1) >> \gamma_L$, the laser width. The factor $(\omega_{p_j'} - \omega_1)$ can therefore be set to the line center value $(\omega_{p_j'} - \omega_{L_1})$ and can be removed from the integral, leaving

$$\begin{aligned} Q_M(\omega) &= G\, A_{M\alpha\beta}\left(\omega,\omega-\omega_{L_1},\omega_{L_1}\right) \int_{-\infty}^{\infty} E_\alpha(\omega-\omega_1) E_\beta(\omega_1) d\omega_1 \\ &= 2G\, A_{M\alpha\beta}\left(\omega,\omega-\omega_{L_1},\omega_{L_1}\right) \mathcal{E}_{\alpha\beta}(\omega) \end{aligned} \qquad \text{(A8)}$$

where $\mathcal{E}_{\alpha\beta}(\omega)$ is the Fourier transform of the product $(E_{1\alpha}(t) \cdot E_{2\beta}(t))$. If the lasers are assumed to have Lorentzian spectral distributions, we have

$$|\mathcal{E}_{\alpha\beta}(\omega)|^2 \propto I_{1\alpha} I_{2\beta} \left\{ \frac{\left(\gamma_{L_1} + \gamma_{L_2}\right)/\pi}{\left(\omega - \omega_{L_1} - \omega_{L_2}\right)^2 + \left(\gamma_{L_1} + \gamma_{L_2}\right)^2} \right\}. \qquad \text{(A9)}$$

The total power radiated by the quadrupole distribution in a particular direction will involve terms proportional to

$$\begin{aligned} \int Q_M^*(t) Q_{M'}(t) dt &= 2\pi \int Q_M^*(\omega) Q_{M'}(\omega) d\omega \\ &= 4G^2 \left(\frac{2\pi}{c}\right)^2 I_1 I_2 \left(\lambda_{1\alpha}^* \lambda_{2\beta}^* \lambda_{1\alpha'} \lambda_{2\beta'}\right) \int A_{M\alpha\beta}^* A_{M'\alpha'\beta'} \left(\omega,\omega-\omega_{L_1},\omega_{L_1}\right) F_L(\omega) d\omega \end{aligned} \qquad \text{(A10)}$$

where $F_L(\omega) = \dfrac{\gamma_L/\pi}{(\omega - \omega_L)^2 + \gamma_L^2}$ for the Lorentzian line case, with $\gamma_L = (\gamma_{L_1} + \gamma_{L_2})$ and $\omega_L = \omega_{L_1} + \omega_{L_2}$, and $\vec{\lambda}_1$ and $\vec{\lambda}_2$ are the electric field polarization vectors.

The function $Z(\eta)$ has approximate forms for large and small $|\eta|$ which aid in approximating the integral in Eq. (A10):

$$|\eta| << 1, \text{ Im } \eta > 0: \quad Z(\eta) \simeq i\sqrt{\eta}\, e^{-\eta^2} - 2\eta\, 1 - \frac{2\eta^2}{3} + \frac{4\eta^4}{15} - \ldots \tag{A11a}$$

$$|\eta| >> 1: \quad Z(\eta) \simeq -\frac{1}{\eta}\, 1 + \frac{1}{2\eta^2} + \frac{3}{4\eta^4} \ldots \quad . \tag{A11b}$$

If we consider a single unsplit level, the integral over frequency in Eq. (A10) is proportional to

$$\frac{1}{\Delta\omega_1^2} \int \frac{|Z(\Delta + i\Gamma)|^2}{\Omega^2} F_L(\omega)\, d\omega \tag{A12}$$

where $\Delta\omega_1 = (\omega_p - \omega_{L_1})$.

If we ignore Doppler broadening ($\Omega \to 0$) Eq. (A11b) shows

$$\left|\frac{Z(\Delta + i\Gamma)}{\Omega}\right|^2 \simeq \frac{1}{(\omega_d - \omega)^2 + \gamma^2}\,, \tag{A13}$$

and the integral (A12) gives the dependence on ω_L

$$\frac{1}{\gamma} \cdot \frac{(\gamma + \gamma_L)}{(\omega_d - \omega_L)^2 + (\gamma + \gamma_L)^2}\,, \tag{A14}$$

and if $\gamma_L >> \gamma$ the maximum power $\mathcal{P}(\omega)$ is reduced by one factor of (γ/γ_L) from its value for two monochromatic lasers. In the Doppler broadened case, the limits of very narrow and very broad laser lines give approxi-

mate expressions for (A12)

$$\gamma_L << \left\{\begin{matrix}\gamma \\ \Omega\end{matrix}\right\}: \frac{1}{\Delta\omega_1^2}\left|\frac{Z(\Delta_L + i\Gamma)}{\Omega}\right|^2 \qquad \Delta_L \equiv (\omega_L - \omega_d)/\Omega \tag{A15a}$$

$$\gamma_L >> \left\{\begin{matrix}\gamma \\ \Omega\end{matrix}\right\}: \frac{1}{\Delta\omega_1^2}\frac{F_L(\omega_d)}{\Omega}\int_{-\infty}^{\infty}|Z(\Delta + i\Gamma)|^2\, d\Delta = \tag{A15b}$$

$$\frac{1}{\Delta\omega_1^2}\frac{F_L(\omega_d)}{\Omega}\cdot\left\{\pi\sqrt{2\pi}[1 - \Phi(\sqrt{2}\Gamma)]e^{2\Gamma^2}\right\}$$

where $\Phi(x)$ is the standard error function. For the usual case where $\Omega >> \gamma$, these have the maximum values π/Ω^2 and $\sqrt{2\pi}/(\gamma_L\Omega)$ respectively.

Our experimental case corresponds most closely to (A15b), since we have $\gamma \simeq 1.5 \times 10^{-3}$ cm^{-1}, Doppler width $\Omega \simeq .085$ cm^{-1} and laser bandwidth $\gamma_L \simeq .25$ cm^{-1}.

If we now consider the effect of fine structure and Zeeman splitting, Eq. (A5) must be used for A. This leads to the replacement of the expression in (A12) by

$$\frac{1}{\Omega^2}\int \sum_{\substack{jj'm \\ j''j'''m'}} \left(W_{jj'm}^{M\alpha\beta}\, W_{j''j'''m'}^{M'\alpha'\beta'}\right)\frac{Z^*(\omega/\Omega - \Omega_{jm}^{M\alpha\beta} + i\Gamma)Z(\omega/\Omega - \Omega_{j''m'}^{M'\alpha'\beta'} + i\Gamma)}{\Delta\omega_1' \qquad\qquad \Delta\omega_1'''} F_L(\omega)\, d\omega \tag{A16}$$

where $\Omega_{jm}^{M\alpha\beta} = [\omega_{d_j} + z_{jm}^{M\alpha\beta}\ \mu_B B/\hbar]/\Omega$ is a normalized transition frequency with $z_{jm}^{M\alpha\beta} = (g_j m_j - g_{\frac{1}{2}} m)$ as a Zeeman splitting factor, and $\Delta\omega_1' = \omega_{p_{j'}} - \omega_{L_1}$, $\Delta\omega_1''' = \omega_{p_{j'''}} - \omega_{L_1}$. The dependence of the output power on B very near resonance can be determined by using Eq.(A11a) for the Z functions, since Γ is small compared to 1. In this approximation Z is a Gaussian. With the additional assumption $\gamma_L >> \Omega$, $F_L(\omega) \approx F_L(\omega_d)$ can be removed from the integral, which can then be evaluated. The result is

$$F_L(\omega_d) \sum_{\substack{jj'm \\ j''j'''m'}} \left(W^{M\alpha\beta}_{jj'm}\, W^{M'\alpha'\beta'}_{j''j'''m'}\right) \cdot \frac{1}{\Delta\omega_1'\Delta\omega_1'''} \cdot \frac{\pi}{\Omega}\sqrt{\frac{\pi}{2}} \cdot \exp[-(\Omega^{M\alpha\beta}_{jm} - \Omega^{M'\alpha'\beta'}_{j''m'})^2/2]. \tag{A17}$$

If the exponential is expanded in powers, we have to lowest order

$$\exp \approx \left(1 - \frac{1}{2\Omega^2}\left[\left(\omega_{d_j} - \omega_{d_{j''}}\right) + \left(z^{M\alpha\beta}_{jm} - z^{M'\alpha'\beta'}_{j''m'}\right)\mu_B B/\hbar\right]^2\right). \tag{A18}$$

If we let $\Delta\omega_{fs}$ be the fine-structure splitting, $(\omega_{d_j} - \omega_{d_{j'}})$ is 0 if $j = j''$ and $\pm\,\Delta\omega_{fs}$ for $j \neq j''$. Then we have the magnetically induced sum-frequency powers linear and quadratic in B, and independent of B proportional to

$$\Delta\omega_{fs}\ \omega_B/\Omega^2 \ :\ \omega_B^2/2\Omega^2 \ :\ 1$$

respectively, where $\omega_B \equiv \mu_B B/\hbar$. The 4d fine-structure splitting for sodium is $\Delta\omega_{fs} = 0.035\ cm^{-1}$. For a B field of 100 Gauss, $\omega_B \simeq 4.7 \times 10^{-3}$ cm^{-1} and the ratios are 2.26×10^{-2} and 1.50×10^{-3}. Since the magnetically induced quadrupole is rotated 90° with respect to the B independent quadrupole, the output powers will also be proportional to $\cos^2\theta_p$ and $\sin^2\theta_p$ respectively. Since θ_p is small, this compensates for the smaller susceptibility for magnetically induced QSFG. For $\theta_p \sim 40$ mrad, the two contributions to $\mathcal{F}(\omega)$ will be equal when B ≃ 10 Gauss. The factors $W^{M\alpha\beta}_{jj'm}$ are given for both the s → d quadrupole and p → p' quadrupole cases in Table I. They are normalized so that $\sum_{jj'm} W^{2,-1,-1}_{j,j',m} = 1$. Table II gives the Zeeman factors $z^{M\alpha\beta}_{jm} = (g_j m_j - g_{j'} m)$ for calculation of the magnetic effect. In the second term of $A^{nn'}_{jj'}$ (Eq. 21) the Zeeman factors for (-m) must be used in the "m" term in the average over ground state spin.

TABLE I. SPIN-ORBIT SPLITTING FACTORS $W^{M\alpha\beta}_{jj'm}$ *

a.) d → s quadrupole transition: $j = j_d$, $j' = j_p$

jj':	5/2 3/2	3/2 3/2	3/2 1/2
$W^{2-1-1}_{jj'm}$	1/2 1/10	0 1/15	0 1/3
$W^{10-1}_{jj'm} = 1/\sqrt{2}\cdot$	-1/5 -2/5	1/30 -1/10	-1/3 0
$W^{1-10}_{jj'm} = 1/\sqrt{2}\cdot$	-1/5 -2/5	-2/15 1/15	-1/6 -1/6
$W^{01-1}_{jj'm} = 1/\sqrt{6}\cdot$	3/10 3/10	-2/15 1/5	1/3 0
$W^{000}_{jj'm} = \sqrt{2/3}\cdot$	3/10 3/10	1/30 1/30	1/6 1/6

b.) p → p quadrupole transition: $j = j_p$, $j' = j'_p$

jj':	3/2 3/2	3/2 1/2	1/2 3/2
$W^{2-1-1}_{jj'm} =$	1/6 1/6	1/3 0	0 1/3
$W^{10-1}_{jj'm} = 1/\sqrt{2}\cdot$	0 -1/3	-1/3 0	-1/6 -1/6
$W^{1-10}_{jj'm} = 1/\sqrt{2}\cdot$	-1/3 0	-1/6 -1/6	0 -1/3
$W^{01-1}_{jj'm} = 1/\sqrt{6}\cdot$	-1/6 1/2	1/3 0	1/3 0
$W^{000}_{jj'm} = \sqrt{2/3}\cdot$	1/6 1/6	1/6 1/6	1/6 1/6

*Top (bottom) value of pair is for m = + 1/2(-1/2). Values not given may be derived using $W^{M\alpha\beta}_{jj'm} = W^{-M-\alpha-\beta}_{jj'-m}$.

TABLE II. ZEEMAN SPLITTING FACTORS $z_{jm}^{M\alpha\beta}$

$\ell'j'$: \ ℓ,j:	$d_{5/2}$	$d_{3/2}$	$p_{3/2}$	$p_{1/2}$
$s_{1/2}$	$-\frac{6}{5}M-\frac{4}{5}m$	$-\frac{4}{5}M-\frac{6}{5}m$	$\frac{4}{3}\beta-\frac{2}{3}m$	$\frac{2}{3}\beta-\frac{4}{3}m$
$p'_{3/2}$	—	—	$\frac{4}{3}M$	$\frac{2}{3}(M-m-\beta)$
$p'_{1/2}$	—	—	$\frac{2}{3}(2M+m+\beta)$	$\frac{2}{3}M$

(m is the spin variable of the ground s state, and takes the value $\pm 1/2$.)

APPENDIX B: SPHERICAL TENSORS

The following definitions follow those given by Tinkham[51] in Group Theory and Quantum Mechanics. The summation convention is assumed.

The spherical basis vectors $\hat{u}_1$, $\hat{u}_0$, and $\hat{u}_{-1}$ defined:

$$\hat{u}_{\pm 1} = \mp \left(\frac{\hat{e}_x \pm i\hat{e}_y}{\sqrt{2}} \right)$$
$$\hat{u}_0 = \hat{e}_z. \tag{B1}$$

These have the scalar product

$$\hat{u}_\alpha \cdot \hat{u}_\beta = (-1)^\alpha \delta_{\alpha,-\beta}. \tag{B2}$$

An arbitrary vector can be expanded:

$$\vec{V} = (-1)^q V_{-q} \hat{u}_q. \tag{B3}$$

V_q is defined by $V_q = \hat{u}_q \cdot \vec{V}$ so that

$$\vec{V} \cdot \vec{W} = V_{-q} W_q (-1)^q. \tag{B4}$$

If we have a set of unit vectors that are rigidly fastened to the physical system we are discussing - an atom for instance - and these vectors are initially coincident with the "lab" basis vectors, then if we rotate the object (with its unit vectors attached), the rotated system basis can be expressed in the fixed lab basis:

$$R\,\hat{u}_{\ell} = \hat{u}_{\ell'}\,R_{\ell'\ell}. \tag{B5}$$

If we use the spherical basis defined by (B1), the matrix R is just the standard quantum mechanical rotation matrix for a spin one particle:

$$R_{\ell'\ell} = D^{(1)}_{\ell'\ell}(\alpha,\beta,\gamma) \tag{B6}$$

where (α,β,γ) are the Euler angles of the rotation.

$$D^{(1)}_{\ell'\ell}(\alpha,\beta,\gamma) = e^{-i\ell'\alpha}\, d^{(1)}_{\ell'\ell}(\beta)\, e^{-i\ell\gamma} \tag{B7}$$

We are concerned now with higher order tensors. We can write an expression for an ordinary Cartesian tensor (for example a fourth rank tensor):

$$\overleftrightarrow{\chi} = \chi_{ijk\ell}\,\hat{e}_i\,\hat{e}_j\,\hat{e}_k\,\hat{e}_{\ell}. \tag{B8}$$

Again the unit vectors initially coincide with the lab vectors, but rotate with the physical system. We may now form a spherical basis tensor

$$\hat{u}_{\alpha}\,\hat{u}_{\beta}\,\hat{u}_{\gamma}\,\hat{u}_{\delta} \tag{B9}$$

where the $\hat{u}$ vectors are composed of the lab Cartesian basis according to (B1), and use it to project out a spherical component of the tensor:

$$\chi_{\alpha\beta\gamma\delta} \equiv \chi_{ijk\ell}(\hat{e}_i \cdot \hat{u}_{\alpha})(\hat{e}_j \cdot \hat{u}_{\beta})(\hat{e}_k \cdot \hat{u}_{\gamma})(\hat{e}_{\ell} \cdot \hat{u}_{\delta}) \tag{B10}$$

so the tensor is now represented

$$\overleftrightarrow{\chi} = (-1)^{\alpha + \beta + \gamma + \delta} \chi_{\alpha\beta\gamma\delta}\, \hat{u}_{-\alpha}\, \hat{u}_{-\beta}\, \hat{u}_{-\gamma}\, \hat{u}_{-\delta}. \tag{B11}$$

The quantity $(\hat{e}_i \cdot \hat{u}_\alpha)$ can be regarded as an element of a matrix which transforms a vector from spherical to Cartesian components, and is explicitly given by

$$\begin{pmatrix} V_x \\ V_y \\ V_z \end{pmatrix} = T \begin{pmatrix} V_{+1} \\ V_0 \\ V_{-1} \end{pmatrix} \qquad T = \frac{1}{\sqrt{2}} \begin{pmatrix} -1 & 0 & 1 \\ -i & 0 & -i \\ 0 & \sqrt{2} & 0 \end{pmatrix} \qquad T^{-1} = T^{+}. \tag{B12}$$

By a simple device we can define combinations of spherical components of a tensor χ which relate tensors of higher rank, and have very simple form. Using the orthogonality of the Clebsch-Gordan coefficients:

$$\sum_{J,M} \begin{pmatrix} j_1 & j_2 & J \\ m_1 & m_2 & M \end{pmatrix} \begin{pmatrix} j_1 & j_2 & J \\ m_1' & m_2' & M \end{pmatrix} = \delta_{m_1 m_1'}\, \delta_{m_2 m_2'} \tag{B13}$$

we write the product of the tensor $\chi_{\alpha\beta}$ and two vectors, for example,

$$\chi_{\alpha\beta} E^1_{-\alpha} E^2_{-\beta} (-1)^{\alpha + \beta} = \chi_{\alpha\beta} \begin{pmatrix} 1 & 1 & J \\ \alpha & \beta & M \end{pmatrix} (-1)^{\alpha + \beta} \begin{pmatrix} 1 & 1 & J \\ \alpha' & \beta' & M \end{pmatrix} E^1_{-\alpha'} E^2_{-\beta'}. \tag{B14}$$

Now we define $\chi^J_M \equiv \chi_{\alpha\beta} \begin{pmatrix} 1 & 1 & J \\ \alpha & \beta & M \end{pmatrix}$

and $$(E^1 E^2)^J_{-M} = \begin{pmatrix} 1 & 1 & J \\ \alpha' & \beta' & M \end{pmatrix} E^1_{-\alpha'} E^2_{-\beta'}. \tag{B15}$$

Then the product of the tensor $\overleftrightarrow{\chi}$ with the two vectors is simply

$$\overleftrightarrow{\chi} : E^1 E^2 = \chi^J_M (E^1 E^2)^J_{-M} (-1)^M. \tag{B16}$$

Following (B5) and (B6) the $\alpha\beta$ component of the tensor corresponding to the

rotated system is:

$$(R\chi)_{\alpha\beta} = \chi_{\gamma\delta}\, D^{(1)}_{\alpha\gamma}\, D^{(1)}_{\beta\delta}. \tag{B17}$$

If we consider the effect of the rotation on χ^J_M, we have

$$(R\chi)^J_M = \chi_{\gamma\delta}\, D^{(1)}_{\alpha\gamma}\, D^{(1)}_{\beta\delta} \begin{pmatrix} 1 & 1 & J \\ \alpha & \beta & M \end{pmatrix}. \tag{B18}$$

But

$$D^{(1)}_{\alpha\gamma}\, D^{(1)}_{\beta\delta} = \sum_{KNN'} \begin{pmatrix} 1 & 1 & K \\ \alpha & \beta & N' \end{pmatrix} \begin{pmatrix} 1 & 1 & K \\ \gamma & \delta & N \end{pmatrix} D^K_{N'N} \tag{B19}$$

and

$$\begin{pmatrix} 1 & 1 & J \\ \alpha & \beta & M \end{pmatrix} \begin{pmatrix} 1 & 1 & K \\ \alpha & \beta & N' \end{pmatrix} = \delta_{JK}\, \delta_{MN'} \tag{B20}$$

so

$$\begin{aligned} (R\chi)^J_M &= \sum_{KNN'} \begin{pmatrix} 1 & 1 & K \\ \alpha & \beta & N' \end{pmatrix} \begin{pmatrix} 1 & 1 & J \\ \alpha & \beta & M \end{pmatrix} \chi_{\gamma\delta} \begin{pmatrix} 1 & 1 & K \\ \gamma & \delta & N \end{pmatrix} D^K_{N'N} \\ &= \chi_{\gamma\delta} \begin{pmatrix} 1 & 1 & J \\ \gamma & \delta & N \end{pmatrix} D^J_{MN} = \chi^J_N\, D^J_{MN}. \end{aligned} \tag{B21}$$

But this is the usual transformation law for a spherical tensor of rank J. Generalizing to a tensor with four indices, we can form

$$\chi^{JJ'}_{MM'} \equiv \chi_{\alpha\beta\gamma\delta} \begin{pmatrix} 1 & 1 & J \\ \alpha & \beta & M \end{pmatrix} \begin{pmatrix} 1 & 1 & J' \\ \gamma & \delta & M' \end{pmatrix} \tag{B22}$$

with rotational transformation properties

$$(R\chi)^{JJ'}_{MM'} = \chi^{JJ'}_{NN'}\, D^{J}_{MN}\, D^{J'}_{M'N'}. \tag{B23}$$

If we have a spherically symmetric system, $\overleftrightarrow{R\chi} = \overleftrightarrow{\chi}$, independent of rotation angle. We exploit this fact by averaging both sides of (B23) over all angles:

$$\chi^{JJ'}_{MM'} = \chi^{JJ'}_{NN'} \int_{-1}^{1} \frac{d(\cos\beta)}{2} \int_{-2\pi}^{2\pi} \frac{d\alpha}{4\pi} \int_{-2\pi}^{2\pi} \frac{d\gamma}{4\pi}\, D^{J}_{MN}\, D^{J'}_{M'N'}(\alpha,\beta,\gamma). \tag{B24}$$

Since the D functions have the orthogonality condition

$$\int_{-1}^{1} \frac{d\cos\beta}{2} \int_{-2\pi}^{2\pi} \frac{d\alpha}{4\pi} \int_{-2\pi}^{2\pi} \frac{d\gamma}{4\pi}\, D^{J}_{MN}\, D^{*J'}_{M'N'} = \frac{\delta_{JJ'}\,\delta_{MM'}\,\delta_{NN'}}{2J+1} \tag{B25}$$

and

$$D^{J'}_{M'N'} = (-1)^{-2J' + M' + N'}\, D^{*J'}_{-M'-N'} \tag{B26}$$

we find

$$\chi^{JJ'}_{MM'} = \chi^{JJ'}_{NN'}\, (-1)^{-2J' + M' + N'}\, \frac{\delta_{JJ'}\,\delta_{M,-M'}\,\delta_{N,-N'}}{2J+1} \tag{B27}$$

$$\chi^{JJ'}_{MM'} = \left(\sum_{N} \frac{\chi^{JJ}_{N-N}(-1)^{-N}}{2J+1} \right) (-1)^{-M}\, (-1)^{-2J'}\, \delta_{JJ'}\, \delta_{M,-M'} \tag{B28}$$

which means for integer J

$$\chi^{JJ'}_{MM'} = \chi^{JJ}_{M-M}\, \delta_{JJ'}\, \delta_{M,-M'} \equiv \chi^{J}(-1)^{M}\, \delta_{JJ'}\, \delta_{M,-M'}. \tag{B29}$$

For the quadrupole susceptibility, J is necessarily 2, and a single number, χ^Q, relates the input fields to the induced quadrupole moment:

$$Q_M = \chi^{2\ 2}_{M-M}(-1)^M(E^1E^2)^2_M = \chi^Q(-1)^M(-1)^M(E^1E^2)^2_M$$
$$= \chi^Q(E^1E^2)^2_M. \tag{B30}$$

The geometric structure of the quadrupole is given directly by the input fields.

Finally, using the orthogonality relation (B13) for the Clebsch-Gordan coefficients, (B22) can be inverted to give

$$\chi_{\alpha\beta\gamma\delta} = \sum_{\substack{JJ' \\ MM'}} \chi^{JJ'}_{MM'} \begin{pmatrix} 1 & 1 & J \\ \alpha & \beta & M \end{pmatrix} \begin{pmatrix} 1 & 1 & J' \\ \gamma & \delta & M' \end{pmatrix}. \tag{B31}$$

For the quadrupole case where only J = 2 enters and M' = -M:

$$\chi_{\alpha\beta\gamma\delta} = \chi^Q \sum_M (-1)^M \begin{pmatrix} 1 & 1 & 2 \\ \alpha & \beta & M \end{pmatrix} \begin{pmatrix} 1 & 1 & 2 \\ \gamma & \delta & -M \end{pmatrix} \tag{B32}$$

$$= \chi^Q(-1)^{\alpha+\beta} \begin{pmatrix} 1 & 1 & 2 \\ \alpha & \beta & (\alpha+\beta) \end{pmatrix} \begin{pmatrix} 1 & 1 & 2 \\ \gamma & \delta & (-\alpha-\beta) \end{pmatrix}. \tag{B33}$$

This shows, for example, that $\chi_{1\ 1-1-1} = \chi^Q$.

As final topic, we note that rather than breaking the four indices of a fourth rank tensor into pairs, as is convenient for the quadrupole susceptibility, it may be more useful to treat three vectors as "inputs" and consider the vector combinations of the three, and the associated susceptibilities. This is the case both for the usual third order processes using $\chi^{(3)}$ and also for second order dipole moments driven by a quadru-

pole transition plus a dipole transition ($s \to d \to p \to s$ for example). The product of the tensor and the three vectors is successively decomposed into the form:

$$P_\alpha = \chi_{\alpha\beta\gamma\delta}(-1)^{\beta+\gamma+\delta} A_{-\beta} B_{-\gamma} C_{-\delta} = \sum_{J,J',\mu} \chi_{\alpha\mu}^{J'}(J)(-1)^{\mu}[A(BC)^J]^{J'}_{-\mu}. \quad (B34)$$

The orthogonality of the Clebsch-Gordan coefficients has been used, as before, and the definitions of the quantities in (B34) are:

$$\chi_{\alpha\mu}^{J'}(J) = \chi_{\alpha\beta M}^{J}\begin{pmatrix}1 & J & J'\\ \beta & M & \mu\end{pmatrix} \quad (B35)$$

$$\chi_{\alpha\beta M}^{J} = \chi_{\alpha\beta\gamma\delta}\begin{pmatrix}1 & 1 & J\\ \gamma & \delta & M\end{pmatrix} \quad (B36)$$

and similarly,

$$[A(BC)^J]^{J'}_{-\mu} = A_{\beta'}[BC]^{J}_{M'}\begin{pmatrix}1 & J & J'\\ -\beta' & -M' & \mu\end{pmatrix} \quad (B37)$$

$$[BC]^{J}_{-M'} = B_{\gamma'} C_{\delta'}\begin{pmatrix}1 & 1 & J\\ -\gamma' & -\delta' & M'\end{pmatrix}. \quad (B38)$$

For isotropic media,

$$\chi_{\alpha\mu}^{J'}(J) = (-1)^{\alpha} \chi^{J} \delta_{\mu,-\alpha} \delta_{J',1} \quad (B39)$$

so if $\vec{P} = \overleftrightarrow{\chi} : \vec{A}\,\vec{B}\,\vec{C}$, we have

$$P_\alpha = \sum_J \chi^J [A(BC)^J]^1_\alpha. \quad (B40)$$

The vectors $[A(\vec{B}\vec{C})^{J}]^{1}$ are explicitly:

$$J = 0: \quad \vec{A}(-1/\sqrt{3})(\vec{B} \cdot \vec{C})$$

$$J = 1: \quad -\vec{A} \times (\vec{B} \times \vec{C})/2 \tag{B41}$$

$$J = 2: \quad \sqrt{3/5}\left\{\vec{A}(\vec{B} \cdot \vec{C})/3 - \vec{B}(\vec{C} \cdot \vec{A})/2 - \vec{C}(\vec{A} \cdot \vec{B})/2\right\}.$$

In a calculation of a susceptibility, J would be the ℓ value for the second intermediate state reached by two dipole transitions.

In the case of a quadrupole pumped process, $B \rightarrow \vec{K}_1$ $C \rightarrow \vec{E}_1$, and only J = 2 is involved, since $(\vec{K}_1 \cdot \vec{E}_1) = 0$ and $(\vec{K}_1 \times \vec{E}_1) \rightarrow \vec{B}_1$ corresponding to a magnetic dipole transition (Pershan).[6]

A more general and more formal discussion of the use of spherical tensors to describe dipole allowed susceptibilities of arbitrary order has been given by Yuratich and Hanna.[52]

APPENDIX C. NOTE ON THE EFFECTS OF SATURATION AND INDUCED REFRACTIVE INDEX CHANGES ON THE MAXIMUM SUM FREQUENCY POWER

Suppose we have a polarization $\vec{P}(\vec{r})$ which has a dominant $\vec{k}$ vector $\vec{k} = \vec{k}_1 + \vec{k}_2 \parallel z$, and frequency $\omega = \omega_1 + \omega_2$. The radiated field is proportional to

$$\vec{A}_{\vec{k}}(\vec{r}) = \frac{e^{ikr}(-i\omega)}{rc} \int e^{-i\vec{k}\cdot\vec{r}'} \vec{P}(\vec{r}')d^3\vec{r}'\Big|_{k_z = \frac{n\omega}{c}} . \qquad (C1)$$

Letting the Fourier transform of $\vec{P}(\vec{r})$ be $\vec{P}_k(\vec{k})$, we see that

$$\vec{A}_{\vec{k}}(\vec{r}) = \frac{e^{ikr}(-i\omega)}{rc} \vec{P}_k(k_x,k_y,\frac{n\omega}{c}) \cdot (2\pi)^3. \qquad (C2)$$

The power distribution is

$$\frac{d\mathcal{P}}{d\Omega} = (\frac{\omega}{c})^4 \frac{c}{2\pi} \vec{P}_k^* \cdot \vec{P}_k(k_x,k_y,\frac{n\omega}{c}) \cdot (2\pi)^6. \qquad (C3)$$

or with $d\Omega = \frac{dk_x dk_y}{k^2}$

$$\mathcal{P}(\Delta k_z) = (\frac{\omega}{c})^4 \frac{(2\pi)^5 c}{k^2} \int \vec{P}_k^* \cdot \vec{P}_k(k_x,k_y,k_z + \Delta k_z)dk_x dk_y \qquad (C4)$$

where $\Delta k_z \equiv (\frac{n\omega}{c} - k_z)$ and it is assumed that the integrand is so sharply packed that $|k|^2 \approx$ constant.

Integrating over Δk_z gives

$$\int \mathcal{P}(\Delta k_z)d\Delta k_z = (\frac{\omega}{c})^4 \frac{(2\pi)^5 c}{k^2} \int \vec{P}_k^*(\vec{k}) \cdot \vec{P}_k(\vec{k})d^3\vec{k}. \qquad (C5)$$

But Parseval's Theorem shows

$$\int \vec{P}_k^*(\vec{k}) \cdot \vec{P}_k(\vec{k}) d^3\vec{k} = \frac{1}{(2\pi)^3} \int \vec{P}^*(\vec{r}) \cdot \vec{P}(\vec{r}) d^3\vec{r}. \tag{C6}$$

So

$$\int \mathcal{P}(\Delta k_z) d\Delta k_z = \left(\frac{\omega}{c}\right)^4 \frac{(2\pi)^2 c}{k^2} \int |\vec{P}(\vec{r})|^2 d^3\vec{r}. \tag{C7}$$

The maximum output power is $\mathcal{P}(\Delta k_z = 0)$. Dividing this out and calling the normalized phase matching curve $\hat{\mathcal{P}}(\Delta k_z)$ we finally obtain

$$\mathcal{P}(\Delta k_z = 0) = \left(\frac{\omega}{c}\right)^4 \lambda^2 c \frac{\int |\vec{P}(\vec{r})|^2 d^3\vec{r}}{\int \hat{\mathcal{P}}(\Delta k_z) d\Delta k_z}. \tag{C8}$$

This formula is interesting because the local effect of saturation is isolated in the numerator, while effects of a nonlocal nature (eg. breaking of phase matching by induced refractive index changes) are isolated in the denominator, and exert their influence by altering the shape of the phase matching curve. The phase matching curve area can be measured experimentally, and we observed broadening from ~ 2 mrad to as much as 14 mrad when defocusing was present.

REFERENCES

1. J. F. Young, G. C. Bjorklund, A. H. Kung, R. B. Miles, and S. E. Harris, PRL 27, 1551 (1971); A. H. Kung, J. F. Young, G. C. Bjorklund, and S. E. Harris, PRL 29, 985 (1972); A. H. Kung, J. F. Young, and S. E. Harris, Applied Physics Letters 22, 301 (1973); D. M. Bloom, G. W. Bekkers, J. F. Young, and S. E. Harris, Applied Physics Letters 26, 687 (1975).
2. J. Reintjes, R. C. Eckardt, C. Y. She, N. E. Karengelen, R. C. Elton, and R. A. Andrews, PRL 37, 1540 (1976); Laser Focus, 14 (Jan. 1977).
3. R. T. Hodgson, P. P. Sorokin, and J. J. Wynne, PRL 32, 343 (1974); P. P. Sorokin, J. J. Wynne, and J. R. Lankard, Appl. Phys. Lett. 22, 342 (1973).
4. J. L. Carlsten and T. J. McIlrath, J. Phys. B 6, L80 (1973); J. L. Carlsten and P. C. Dunn, Opt. Comm. 14, 8 (1975).
5. S. E. Harris and D. M. Bloom, Appl. Phys. Lett. 24, 229 (1974).
6. P. S. Pershan, Phys. Rev. 130 , 919 (1963).
7. Hung Cheng and P. B. Miller, Phys. Rev. 134, A683 (1964).
8. S. S. Jha, Phys. Rev. 140, A2020 (1965).
9. N. Bloembergen and Y. R. Shen, Phys. Rev. 141, 298 (1966).
10. N. Bloembergen, R. K. Chang, S. S. Jha, and C. H. Lee, Phys. Rev. 174, 813 (1968).
11. J. Rudnick and E. A. Stern, Phys. Rev. B4, 4274 (1971).
12. C. S. Wang, J. M. Chen, and J. R. Bower, Opt. Comm. 8, 275 (1973).
13. F. Brown, R. E. Parks, and A. M. Sleeper, PRL 14, 1029 (1965); F. Brown and R. E. Parks, PRL 16, 507 (1966).
14. H. Sonnenberg and H. Heffner, J. Opt. Soc. Am. 58, 209 (1968).

15. C. C. Wang and A. N. Duminski, PRL 20, 668 (1968).

16. T. Hänsch and P. Toschek, Z. Phys. 236, 373 (1970).

17. A. Flusberg, T. Mossberg, and S. R. Hartmann, PRL 38, 59

18. N. Bloembergen, Nonlinear Optics, Benjamin, New York (1965); J. Fiutak, Can. J. Phys. 41, 12 (1963).

19. E. Adler, Phys. Rev. 134, A728 (1964).

20. P. N. Butcher, Nonlinear Optical Phenomena, p. 97, University Engineering, Columbus (1965).

21. U. Fano and G. Racah, Irreducible Tensorial Sets, Academic Press, New York (1965).

22. D. W. Shore and B. Menzel, Principles of Atomic Spectra, J. Wiley and Sons, Inc., New York (1968).

23. A. R. Edmonds, Angular Momentum in Quantum Mechanics, Princeton University Press, Princeton, N. J. (1957).

24. R. B. Miles and S. E. Harris, IEEE J. Quant. Electron. 9, 470 (1973).

25. E. C. Tull, M. Jackson, R. P. McEachran, and M. Cohen, Can. J. Phys. 50, 1169 (1972).

26. C. R. Vidal and J. Cooper, J. Appl. Phys. 40, 3370 (1969).

27. H. Rosen and P. Robrish, Rev. Sci. Instrum. 46, 1115 (1975).

28. J. F. Ward and A. V. Smith, PRL 35, 653 (1975).

29. C. C. Wang and L. I. Davis, PRL 35, 653 (1975).

30. J. N. Elgin and G. H. C. New, Opt. Comm. 16, 242 (1976).

31. W. L. Wiese, M. W. Smith, and B. M. Miles, Atomic Transition Probabilities Vol. II, Natl. Stand. Ref. Data Ser., Nat. Bur. Stand. (U. S.), No. 22 (Oct. 1969).

32. D. Grischkowsky, M. M. T. Loy and P. F. Liao, Phys. Rev. A12, 2514

(1975).

33. B. Couillaud and A. Ducasse, PRL 35, 1276 (1976).

34. P. F. Liao and G. C. Bjorklund, PRL 36, 584 (1976).

35. A. Yariv, Quantum Electronics 2nd Edition, p. 153, J. Wiley and Sons, New York (1975).

36. D. Grischkowsky and J. A. Armstrong, Phys. Rev. A6, 1566 (1972).

37. R. H. Lehmberg, J. Reintjes, and R. C. Eckardt, Phys. Rev. A13, 1095 (1976).

38. S. A. Ahkmanov, A. P. Sukhorukov, and R. V. Khokhlov, Sov. Phys. Uspekhi 10, 609 (1968).

39. T. B. Lucatorto and T. J. McIlrath, PRL 37, 428 (1976).

40. M. R. Teague and P. Lambropoulos, J. Phys. B9, 1251 (1976).

41. L. L. Boyle and J. Murray, J. Phys. B2, 433 (1969).

42. M. P. Bogaard and B. J. Orr, Molec. Phys. 14, 557 (1968).

43. B. Warner, Mon. Not. Roy. Astr. Soc. 139, 115 (1968).

44. M. Lambropoulos, S. F. Moody, S. J. Smith, and W. C. Lineberger, PRL 35, 159 (1975).

45. D. S. Bethune, R. W. Smith, and Y. R. Shen, PRL 37, 431 (1976).

46. See, for example, J. F. Ward and I. J. Bigio, Phys. Rev. A11, 60 (1975); R. S. Finn and J. F. Ward, PRL 26, 285 (1971).

47. M. A. Bouchiat and L. Pottier, J. Physique-Letters 36, L-189 (1975); S. Chu, E. D. Commins, and R. Conti, Phys. Lett. 60A, 96 (1977).

48. $\langle 3s|zz|rd\rangle = (2/\sqrt{45})\langle 3s|r^2|4d\rangle$

$$\equiv (2/\sqrt{45}) \int_0^\infty R_{3s}\, r^2\, R_{4d}\, dr$$

where the radial function for the state $|n\ell\rangle$ is $(R_{n\ell}/r)$.

49. Y. R. Shen, Phys. Rev. 167, 818 (1968).

50. B. D. Fried and S. D. Conte, The Plasma Dispersion Function, Academic Press (1961).

51. M. Tinkham, Group Theory and Quantum Mechanics, (McGraw-Hill, N.Y., S.F., London, 1964).

52. M. A. Yuratich and D. C. Hanna, J. Phys. B9, 729 (1976).

FIGURE CAPTIONS

Fig. 1 Radiation pattern for quadrupole $\overleftrightarrow{Qd}^{3\rightarrow}\hat{x}$ with only $Q_{yz} = Q_{zy} \neq 0$.

Fig. 2 Partial level diagram of the sodium atom. Quadrupole sum-frequency generation with $\omega_3 = \omega_2 + \omega_1$ is shown schematically.

Fig. 3 Experimental set up. PD1, PD2, PD3 - monitor photodetectors, L_1, L_2 - 40 cm and 50 cm lenses; L_3 - 10 cm quartz lens; PR - polarization rotator; F - Corning 7-54 filter and pyrex attenuators; S - 1/4 m. spectrometer; PM - RCA 4837; G.I. - gated integrator; CR - chart recorder.

Fig. 4 Sum-frequency output $P(\omega_3)$ as a function of ω_2 showing the sharp resonance at $\omega_1 + \omega_2 = \omega_{4d} = 34548.8\ cm^{-1}$. $P_1 = 2W$; $P_2 = 25W$; $\theta = 47.9$ mrad; $N = 1.6 \times 10^{16}\ cm^{-3}$.

Fig. 5 Phase-matching curve $P(\omega_3)$ versus θ. $P_1 = 2W$; $P_2 = 25W$; $\Delta\omega_1 \equiv (\omega_{3p_{1/2}} - \omega_1) = +25.6\ cm^{-1}$; $\omega_1 + \omega_2 = \omega_{4d}$; $N = 1.6 \times 10^{16}\ cm^{-3}$. The dashed curve is a theoretical curve calculated from Eq. (33), with $\sigma_1 = \sigma_2 = 0.1$ mm used to derive d.

Fig. 6 Phase matching angle θ_p versus the sodium density N at $\omega_1 + \omega_2 = \omega_{4d}$ and (a) $\Delta\omega_1 = +14.9\ cm^{-1}$; (b) $\Delta\omega_1 = +40.8\ cm^{-1}$; (c) $\Delta\omega_1 = +80.4\ cm^{-1}$. The dots are the data points and the curves are calculated from Eq. (35).

Fig. 7 Normalized output power $\mathcal{P}(\omega_3)/\mathcal{P}(\omega_2)$ versus $\mathcal{P}(\omega_1)$ and $\mathcal{P}(\omega_3)/\mathcal{P}(\omega_1)$ versus $\mathcal{P}(\omega_2)$. p = 1.0 torr, $\Delta\omega_1 = 21.2\ cm^{-1}$.

Fig. 8 Phase-matched sum-frequency output $P(\omega_3)$ as a function of sodium density N at $\Delta\omega_1 = +40.8\ cm^{-1}$ and $+80.4\ cm^{-1}$. The other parameters fixed in the experiment are $P_1 \simeq 2W$, $P_2 \simeq 20W$, and $\omega_1 + \omega_2 = \omega_{4d}$.

Fig. 9 (a) Sum frequency power $\mathcal{P}(\omega_3)$ and (b) resonance linewidth $\Delta\omega_2$ as functions of the product of the input intensities $I_1 I_2$. The solid curves are both derived from Eq. (48) for the effects of two-photon saturation with $\beta^2 = (4.6 \times 10^{-25}) I_1 I_2$ esu.

Fig. 10 Experimental set-up for measuring divergence angle θ_B of beam 1 after heat pipe. PD1 and PD2 are photodetectors. Pinhole diameter is 0.5 mm.

Fig. 11 (a) Solid circles - measured increase of divergence of pump beam 1 after heat pipe as a function of detuning $\Delta\omega_1 = (\omega_{3p_{1/2}} - \omega_1)$. Curve is derived from Eq. (50) with overall normalization adjusted for best fit to data points.

(b) Measured divergence of beam 1 (solid circles) and sum frequency power $\mathcal{P}(\omega_3 = \omega_1 + \omega_2)$ (open circles) as functions of the pump intensity I_1. The dashed curve is the prediction of Eq. (48) for the output power with two-photon saturation taken into account. Additional reduction of power is attributed to induced index of refraction change and self-defocusing (see text).

Fig. 12 Experimental geometry for sum-frequency generation. The dc field $\vec{E}_0$ and the laser field $\vec{E}_1$ are both along $\hat{y}$.

Fig. 13 $I_x(\omega_3)/I_y(\omega_3)$ as a function of the applied dc field E_0 for linear polarized input beams. $I_x(\omega_3)$ and $I_y(\omega_3)$ are phase-matched sum-frequency signals polarized along $\hat{x}$ and $\hat{y}$ respectively. The solid curve is a theoretical curve obtained from Eq. (64) to fit the data points.

Fig. 14 $I_x(\omega_3)/I_y(\omega_3)$ as a function of the applied dc field E_0 for $E(\omega_1)$ linearly polarized along $\hat{y}$ and $E(\omega_2)$ left circularly polarized.

Figure 1

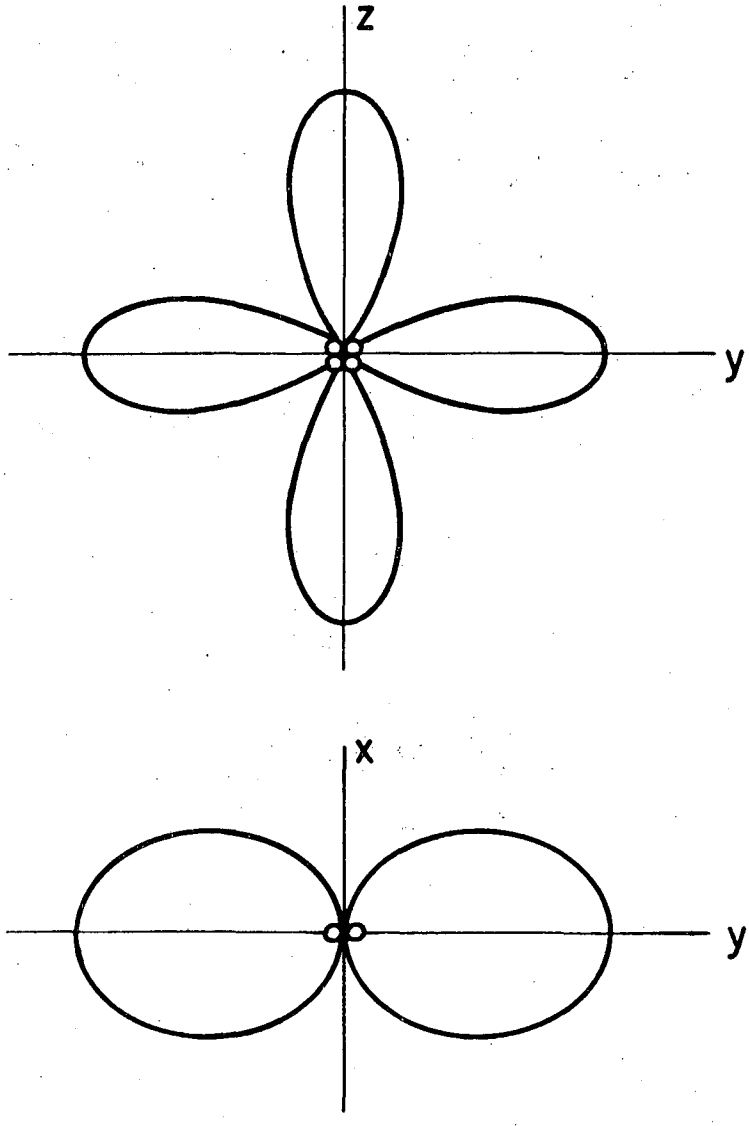

XBL772-5041

Figure 2

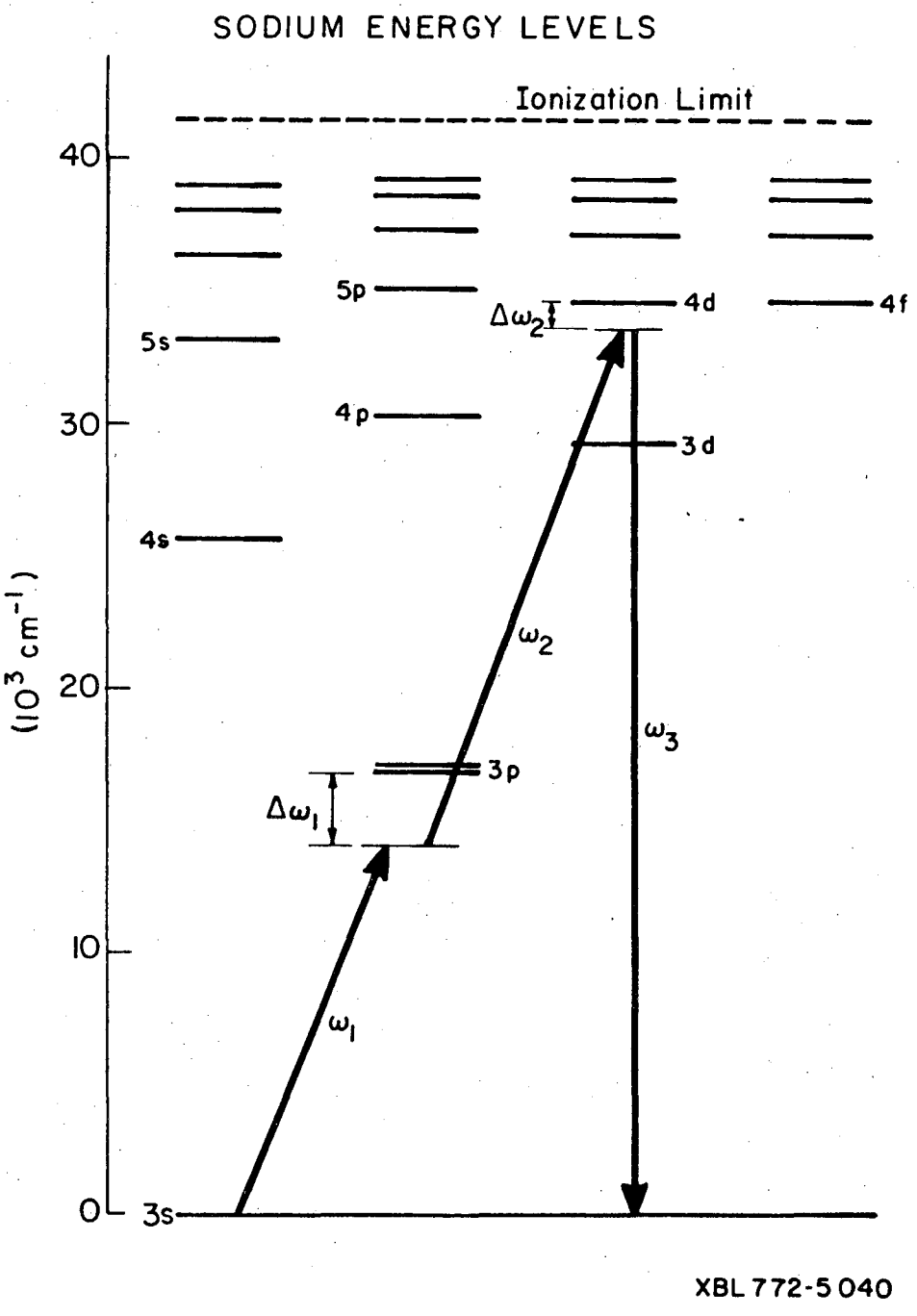
SODIUM ENERGY LEVELS
Ionization Limit
40
30
20
10
0
$(10^3\ cm^{-1})$
5s
5p
4s
4p
3s
3p
3d
4d
4f
$\Delta\omega_2$
$\Delta\omega_1$
ω_1
ω_2
ω_3
XBL 772-5040

Figure 3

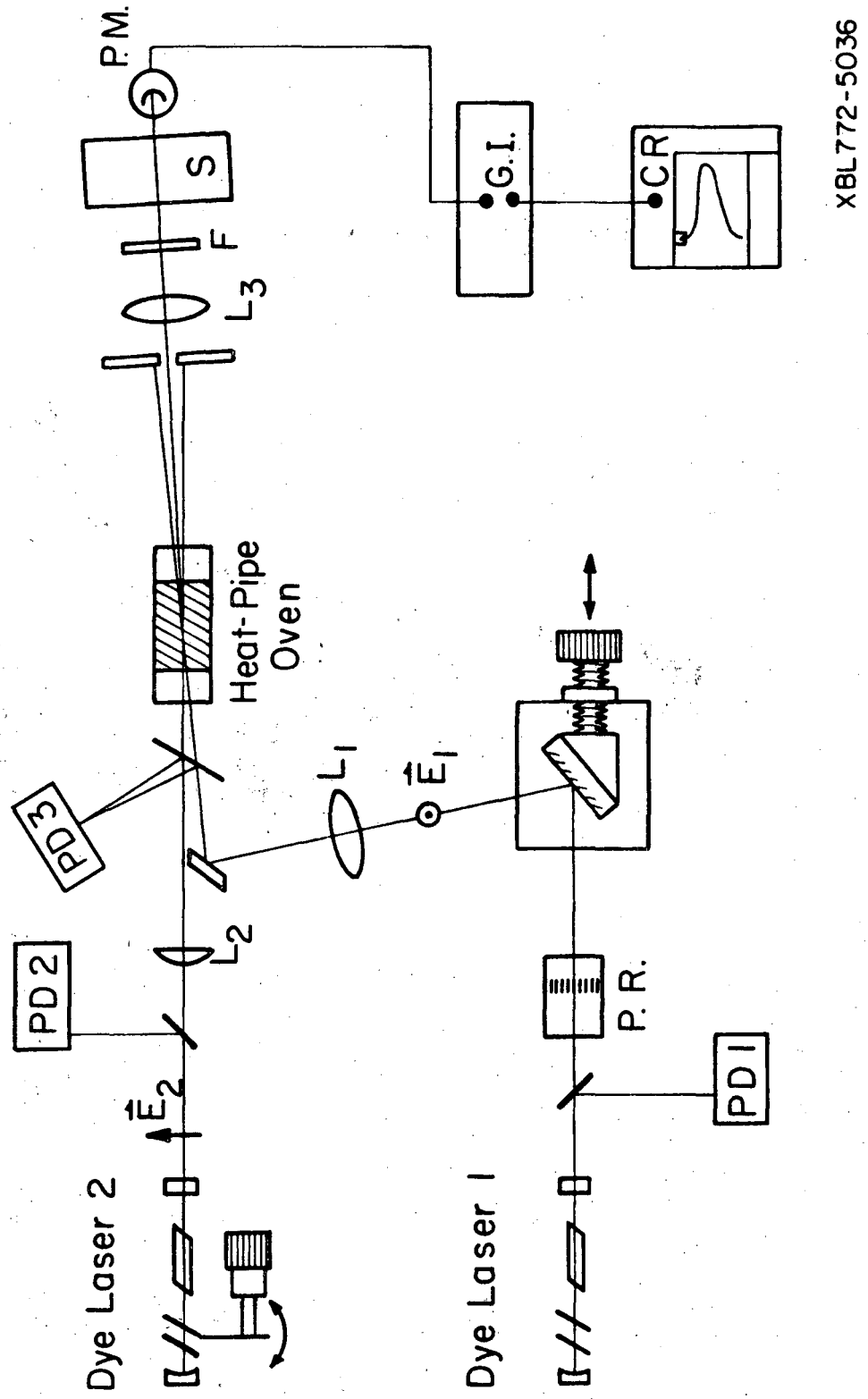

Figure 4

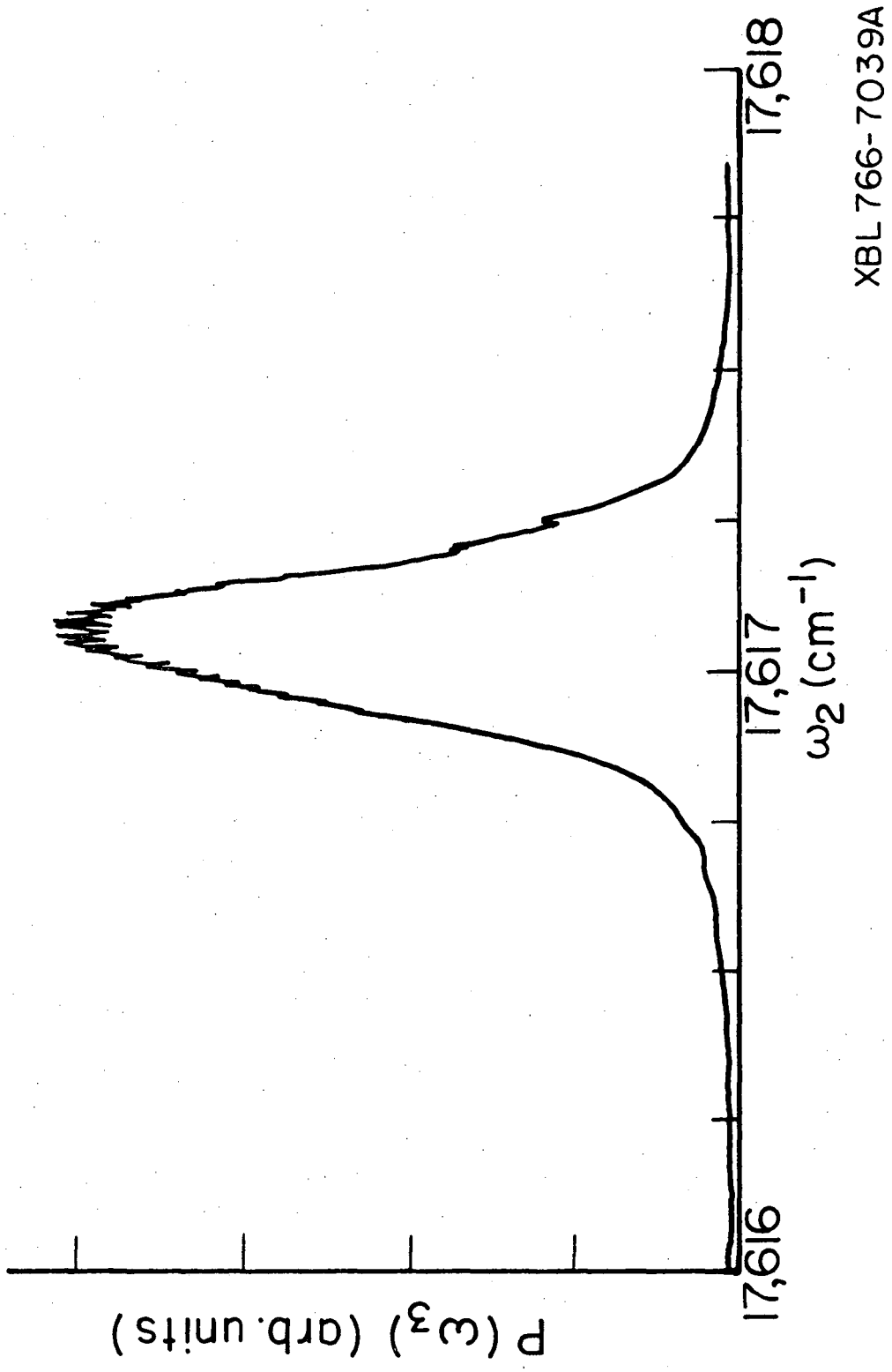

Figure 5

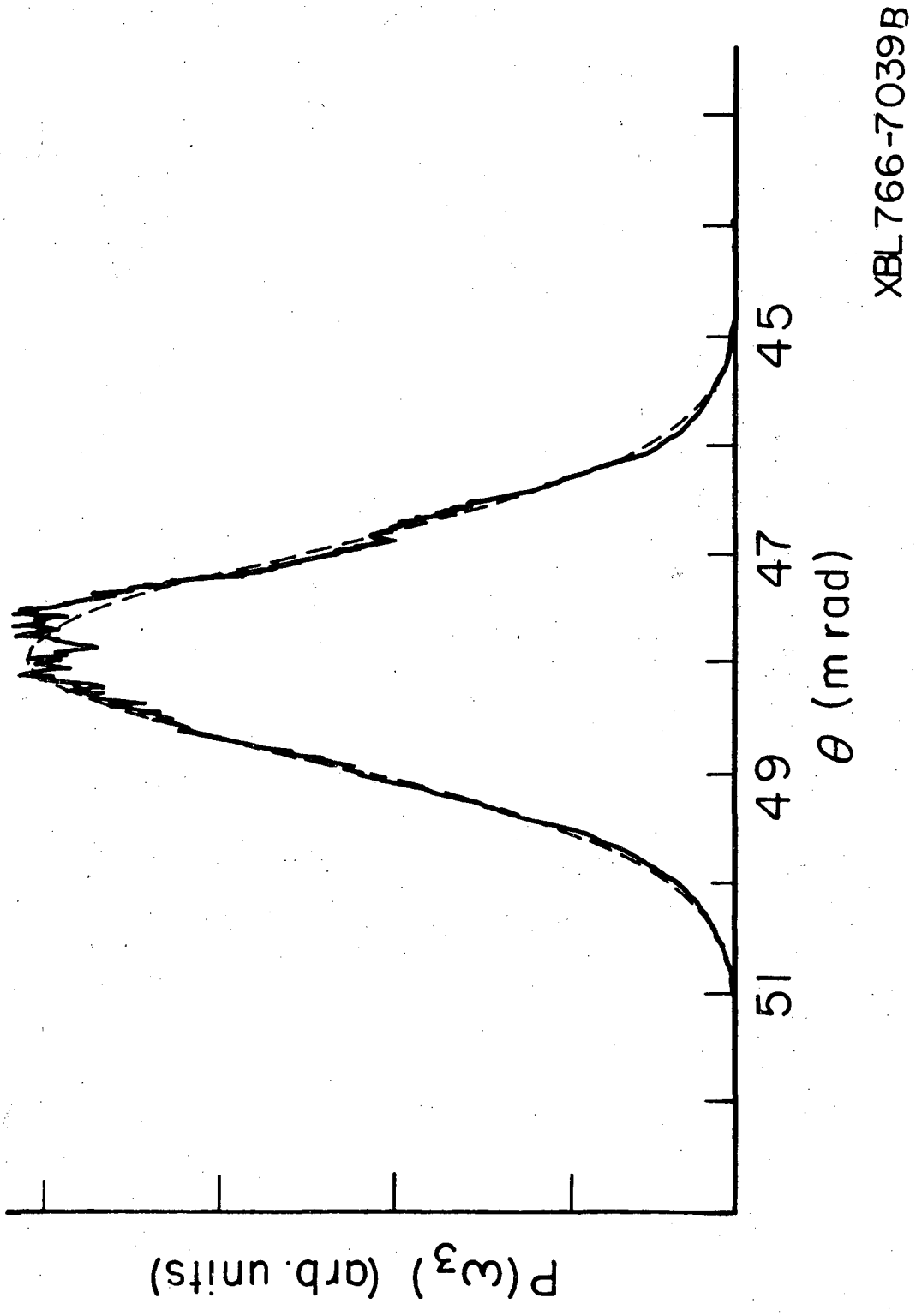

Figure 6

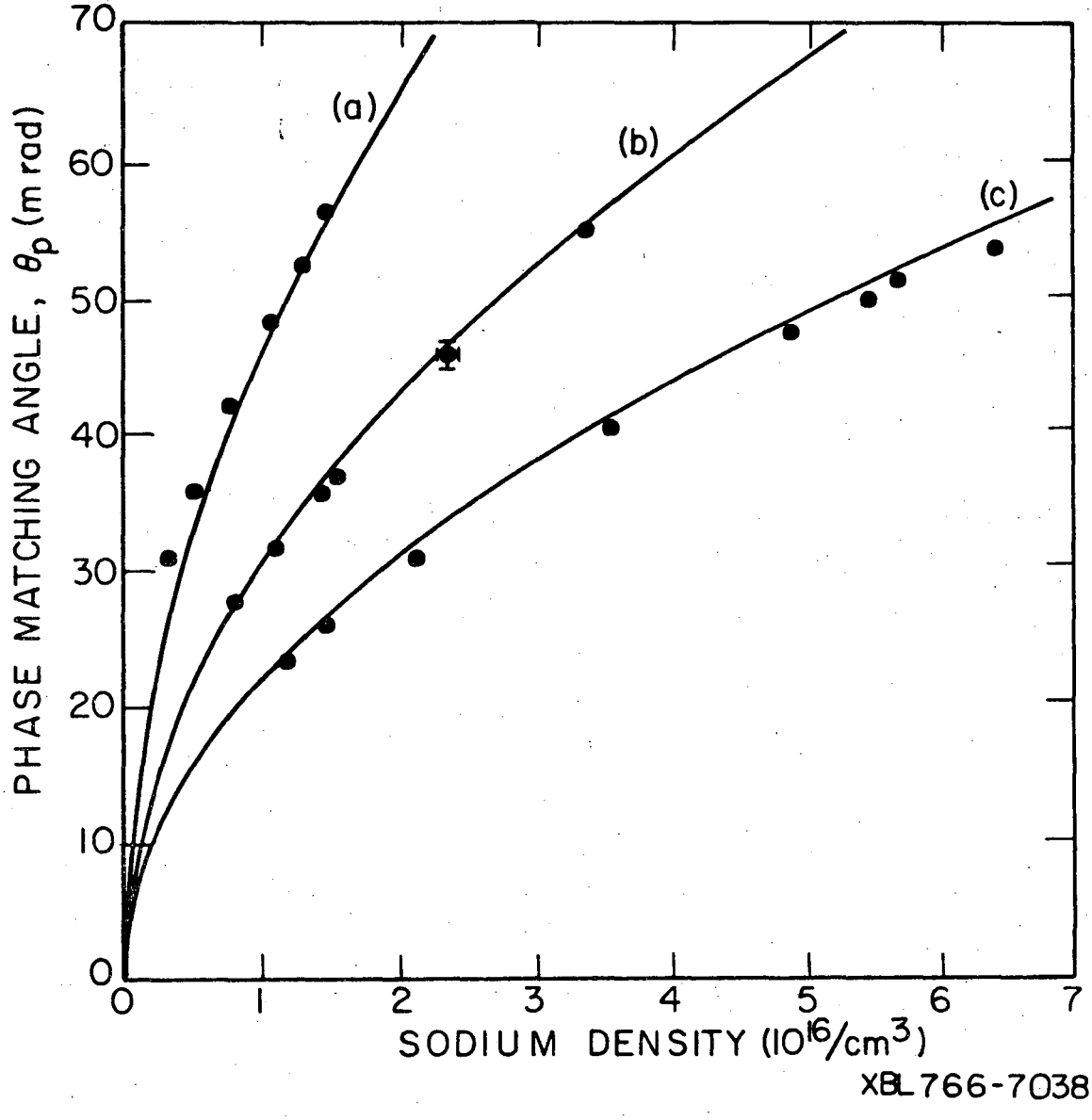
70
60
50
40
30
20
10
0
0
1
2
3
4
5
6
7
(a)
(b)
(c)
PHASE MATCHING ANGLE, θ_p (m rad)
SODIUM DENSITY (10^{16}/cm^3)
XBL766-7038

Figure 7

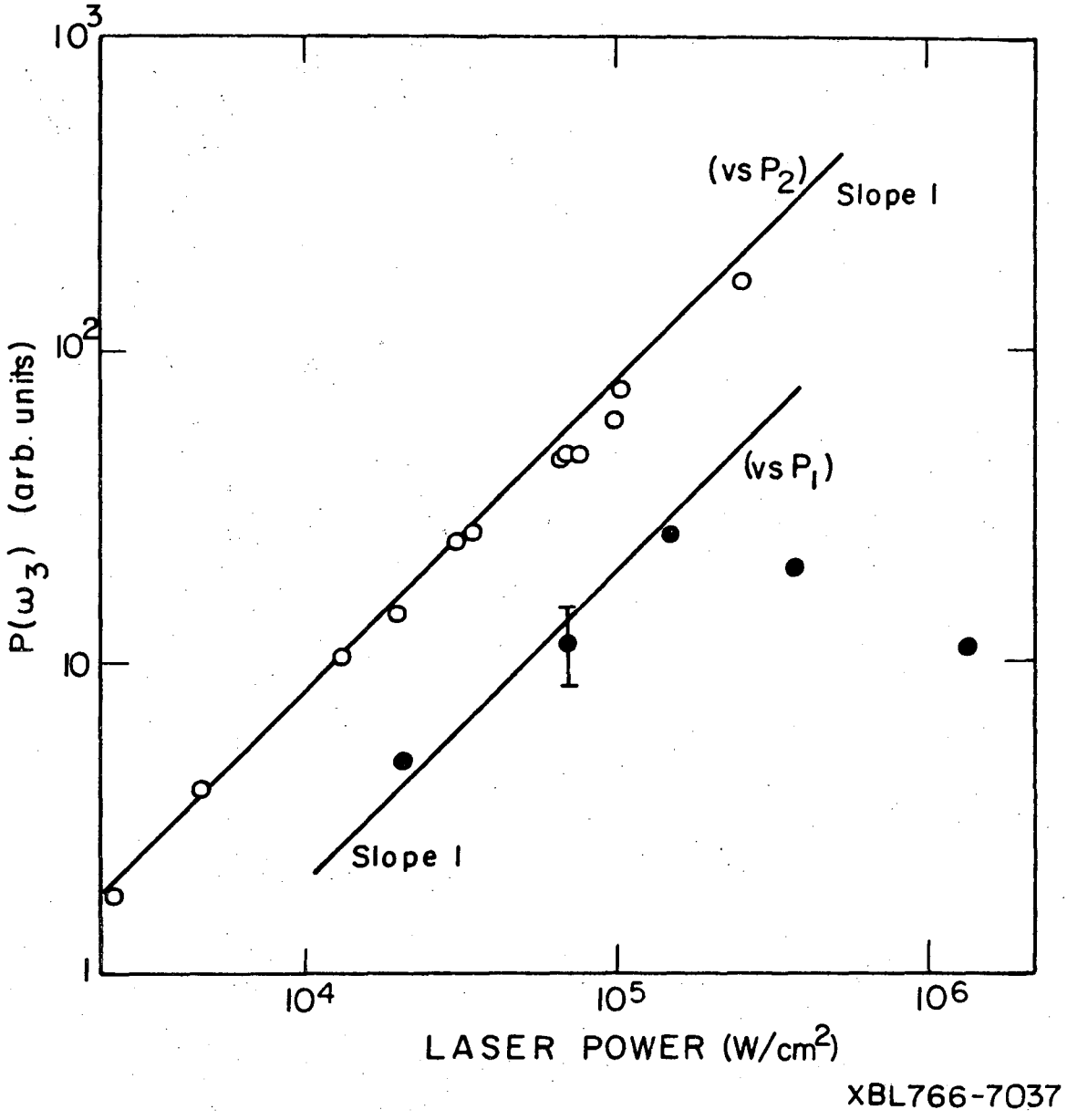

Figure 8

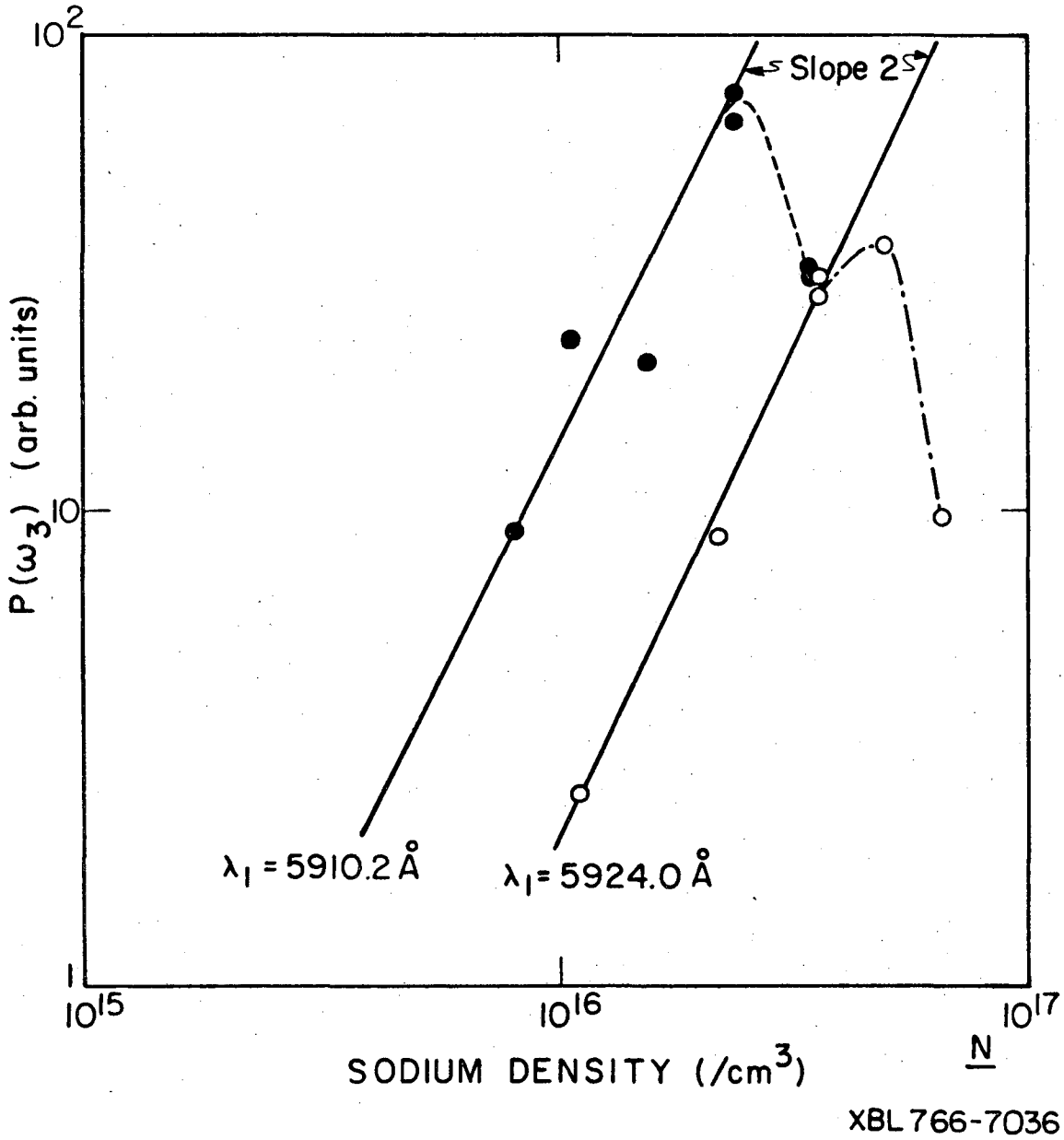
10^2
Slope 2
$P(\omega_3)$ (arb. units)
10
1
λ_1 = 5910.2 Å
λ_1 = 5924.0 Å
10^{15}
10^{16}
10^{17}
SODIUM DENSITY (/cm^3)
N
XBL766-7036

Figure 9

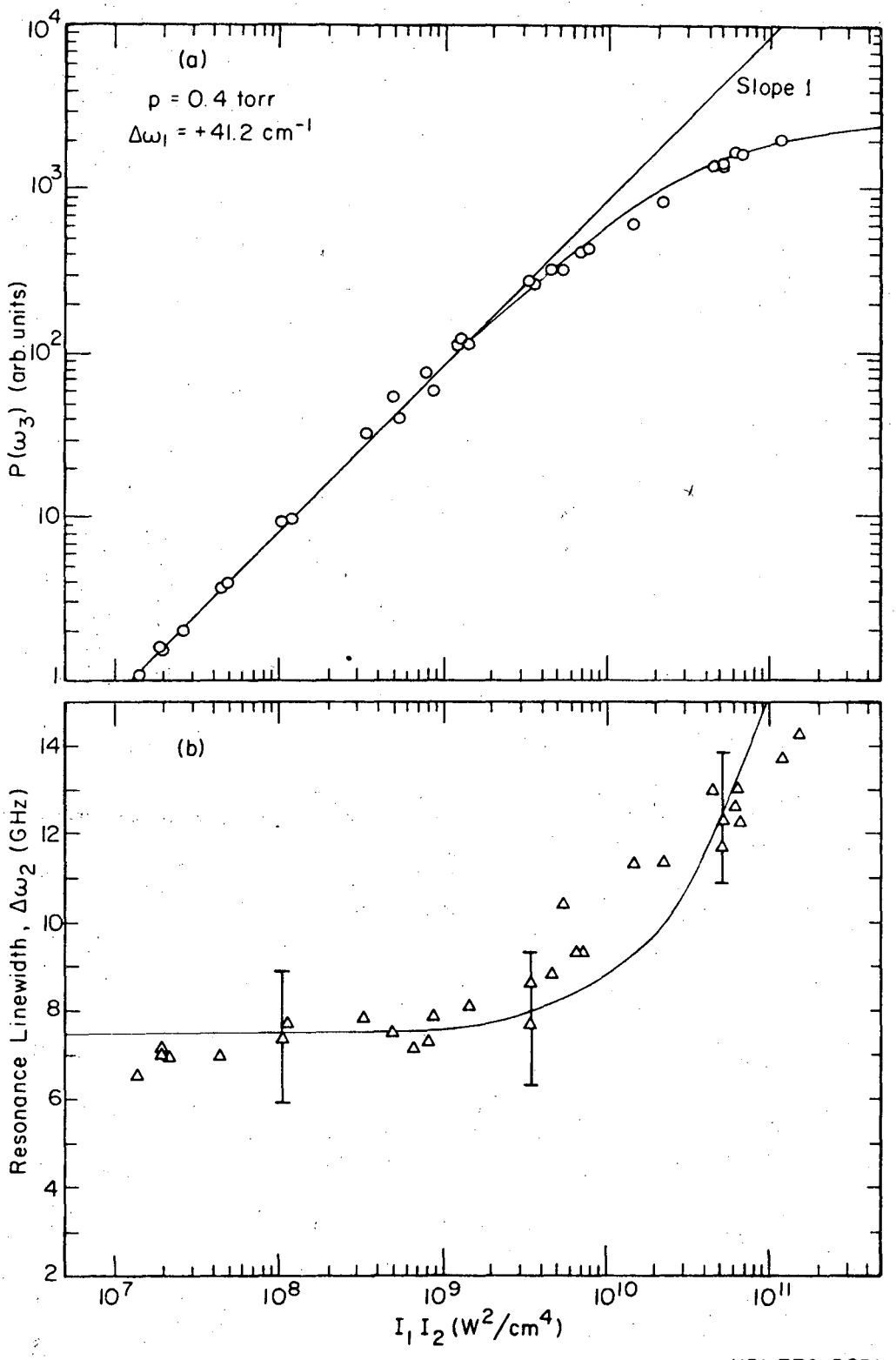

Figure 10

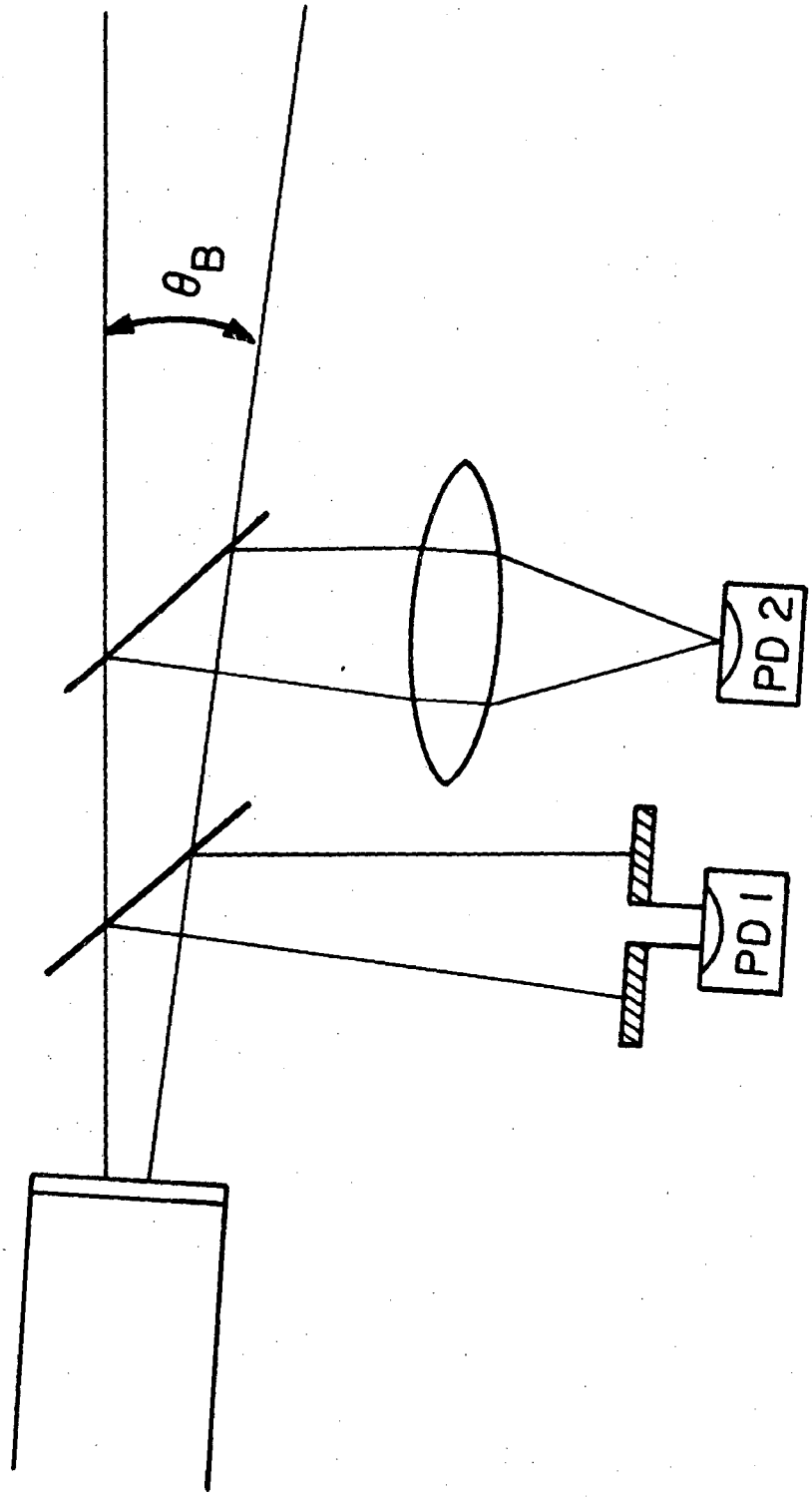

XBL772-5035

Figure 11

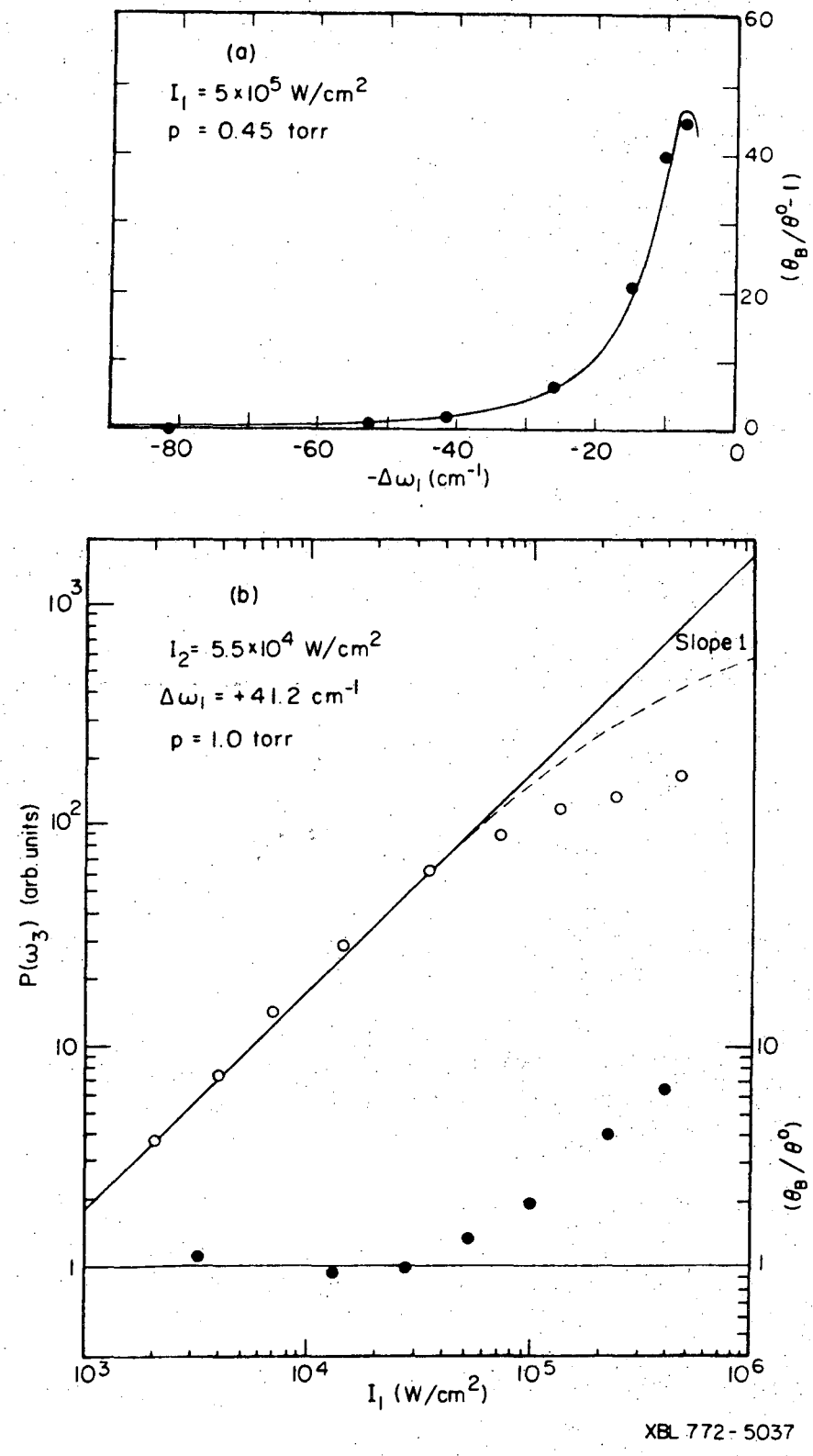

Figure 12

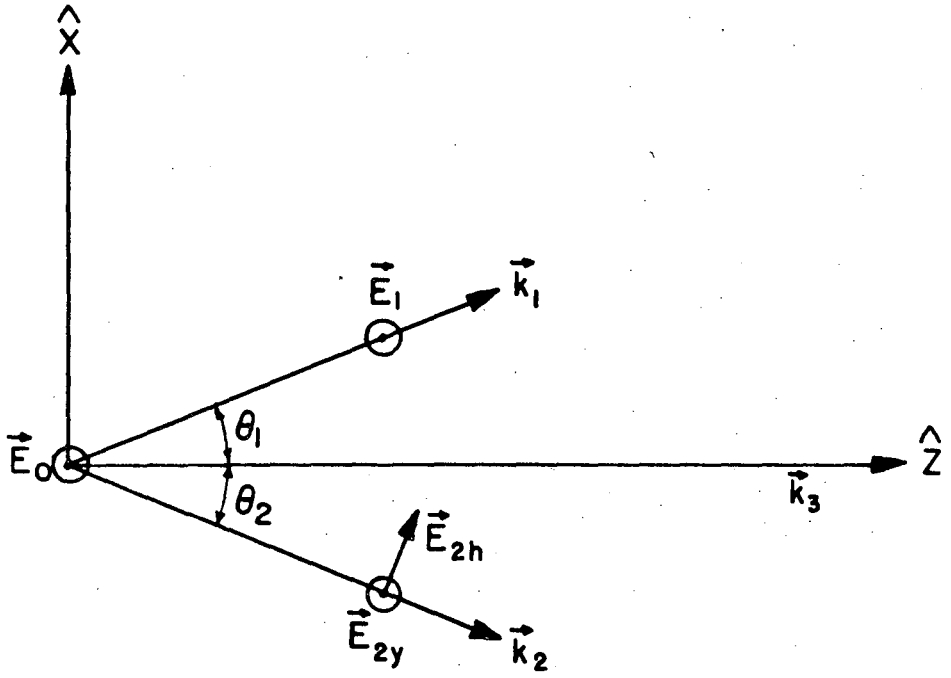

XBL771-4948

Figure 13

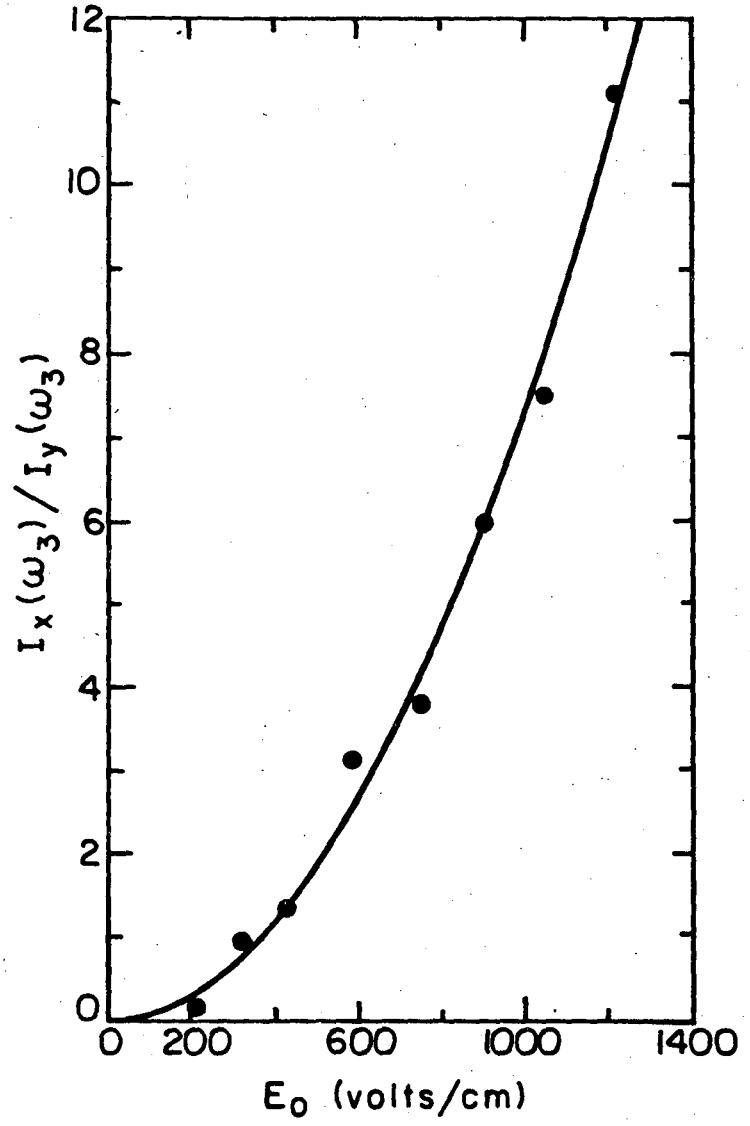

XBL 771-4949

TECHNICAL INFORMATION DIVISION
LAWRENCE BERKELEY LABORATORY
UNIVERSITY OF CALIFORNIA
BERKELEY, CALIFORNIA 94720